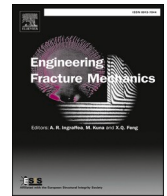




ELSEVIER

Contents lists available at ScienceDirect

Engineering Fracture Mechanics

journal homepage: www.elsevier.com/locate/engfracmech

Anti-plane Yoffe-type crack in flexoelectric material

Ch. Knisovitis^{a,*}, A.E. Giannakopoulos^a, Ares J. Rosakis^b^a Department of Mechanics, School of Applied Mathematical and Physical Sciences, National Technical University of Athens, Athens, Greece^b Graduate Aerospace Laboratories, California, Institute of Technology, Pasadena, CA, USA

ARTICLE INFO

Keywords:

Anti-plane Fracture
Yoffe Problem
Flexoelectricity
Crack tip displacement
Polarization

ABSTRACT

This work investigates the deformation and polarization fields around a finite anti-plane shear (mode III) crack growing dynamically under steady-state conditions. The leading tip of this finite crack breaks the material while the trailing tip heals it. This fast moving finite crack (referred to as a rupture “pulse” in the geophysics literature) propagates with a constant velocity and with the mechanical and the electrical fields that remain invariant with respect to an observer moving with the crack-tips. This problem belongs to the first type of steady state crack growth problems according to the classification of Freund. The “prototype” problem which refers to an isotropic, body subjected to fracture under tensile loading was first proposed and solved by Yoffe, while finite cracks (or shear pulses) were also analyzed by Freund and by Rice. In the above cases the material was assumed to be linear elastic. Our analysis extends these studies to flexoelectric materials, and it is both theoretical and numerical. It discusses the asymptotic structure of the crack-tip displacement and the polarization fields; it calculates the dynamic energy release rate and presents their dependence on crack-tip velocity. Comparisons are made to the available, classical, elasto-dynamic solutions and to the static case. The influence of the electrical properties of the material on strengthening is also analyzed. Dynamic fracture of flexoelectric materials is of relevance to both the study of earthquake source mechanics and to the analysis of the reliability of micro-electronic devices. This is because both rocks and ceramics are flexoelectric. Indeed, during earthquake rupture processes, dynamic, in-plane shear (Mode-II) and out of plane shear (Mode-III), cracks propagate along faults and exhibit both mechanical and electrical polarization signatures. At an entirely different length scale, flexoelectric ceramics are currently used as sensors and transducers and can experience dynamic shear failure along interfaces when subjected to dynamic loading (e.g. impact.). Failure by dynamic fracture can be detrimental to both their mechanical reliability and electrical functionality.

1. Introduction

Flexoelectricity is the ferroelectric effect during which strain gradients applied in a material particle, produce electric polarization and vice versa. As might be expected, the presence of non – uniform strain fields enhance this effect in areas featuring the highest strain gradients. Examples of such fields are found at the near-tip regions of dynamically growing opening (Mode-I) cracks and shear (Mode-II/Mode-III) ruptures, where singular strains and strain gradients, are typically encountered [1–3].

The mode III Yoffe-type problem is an anti-plane Griffith-type crack (Mode-III anti-plane shear rupture) problem involving a

* Corresponding author.

E-mail address: chriskn001@mail.ntua.gr (Ch. Knisovitis).

<https://doi.org/10.1016/j.engfracmech.2024.110551>

Received 10 July 2024; Received in revised form 8 October 2024; Accepted 10 October 2024

Available online 15 October 2024

0013-7944/© 2024 Elsevier Ltd. All rights are reserved, including those for text and data mining, AI training, and similar technologies.

Nomenclature

a	Half Crack Length [m]
a_s	Parameter of the Classical Yoffe Problem [–]
a_0	Atomistic Radius [m]
A_1	Parameter used in the polarization Analysis [–]
A_2	Parameter used in the polarization Analysis [$m^{-1/2}$]
\tilde{A}	Parameter used in the polarization Analysis [–]
b	Asymptotic Angular Variation Displacement Amplitude of First Order [–]
b_1, b_2	Section Dimensions in the Finite Element Method (FEM) Implementation [m]
$(b_{44} + b_{77})$	Gradient Polarization Constant [Nm^4C^{-2}]
B	Asymptotic Angular Variation Displacement Amplitude of Order 3/2 [$m^{-1/2}$]
$B_{classic}$	Classical Yoffe Problem's Asymptotic Angular Variation Displacement Amplitude [$m^{1/2}$]
B_1	Polarization Angular Variation of first order [Cm^{-3}]
B_2	Polarization Angular Variation of order 3/2 [$Cm^{-7/2}$]
\tilde{B}	Parameter used in the polarization Analysis [–]
c_s	Shear Wave Velocity [ms^{-1}]
C	Parameter used in the polarization Analysis [Cm^{-3}]
e_{44}	Inverse Flexoelectric Constant [NmC^{-1}]
f	Asymptotic Angular Variation Displacement of First Order [–]
f_{12}	Flexoelectric Constant [NmC^{-1}]
F	Asymptotic Angular Variation Displacement of Order 3/2 [–]
$F_{classic}$	Classical Asymptotic Angular Variation Displacement [–]
$H/\sqrt{12}$	Equivalent Micro-Inertial Length [m]
\mathfrak{S}	Energy Release Rate [Nm^{-1}]
\mathfrak{S}_c	Critical Energy Release Rate [Nm^{-1}]
$\mathfrak{S}_{classic}$	Energy Release Rate for the Classical Yoffe Problem [Nm^{-1}]
$\mathfrak{S}_{classic,static}$	Energy Release Rate for $V = 0ms^{-1}$ for the Classical Yoffe Problem [Nm^{-1}].
\mathfrak{S}_{static}	Energy Release Rate for $V = 0ms^{-1}$ [Nm^{-1}]
K_{III}	Stress Intensity Factor [$Nm^{-3/2}$]
$K_{III,static}^{classic}$	Classical, Static Yoffe Problem's Stress Intensity Factor [$Nm^{-3/2}$]
$\ell/\sqrt{2}$	Equivalent Microstructural Length [m]
L	Crack Length [m]
$\vec{n} = (n_{x_1}, n_{x_2})$	Normal Unit Vector [–]
P_{max}	Material's Maximum Polarization [Cm^{-2}]
P_3	Out of Plane Polarization [Cm^{-2}]
P_3^{max}	Material's Maximum Polarization in the out of plane direction [Cm^{-2}]
Q	$= \mathfrak{S}/(B^2\mu\ell^2)$, Normalized Energy Release Rate [–]
r	Near Tip Polar Coordinates (radial coordinate)[m]
R	Cohesive Zone Length [m]
t	Time [s]
u_3	Out of Plane Displacement [m]
u_{3max}	Maximum Displacement Along the Crack Length [m]
U	Total Energy Density [Nm^{-2}]
V	Crack Tip Steady State Velocity [ms^{-1}]
x_1	In-Plane Global coordinate (parallel to the crack length coordinate)[m]
x_2	In-Plane Global coordinate (vertical to the crack length coordinate)[m]
α	Reciprocal Dielectric Constant [Nm^2C^{-2}]
$\epsilon_{\theta z}$	Strain in the Tangential to the Radius Direction [–]
$\epsilon_{\theta z}^c$	Critical Strain in the Tangential to the Radius Direction [–]
η	Galerkin's Coordinate System (vertical to the crack length coordinate)[m]
θ	Near Tip Polar Coordinates (angular coordinate)[–]
θ_r	The Slope for Which $F(\theta = \theta_r; \lambda) = 0$ [–]
θ_s	Parameter of the Classical Yoffe Problem [–]
λ	$(V^2/c_s^2)(H^2/6\ell^2)$ [–]
Λ	Parameter used in the polarization Analysis [–]

μ	Shear Modulus [Nm ⁻²]
ξ	Galerkin's Coordinate System (parallel to the crack length coordinate)[m]
ρ	Material Density [kgm ⁻³]
σ_0	Constant Cohesive Stress [Nm ⁻²]
τ_0	Out of Plane Shear Stress [Nm ⁻²]
τ_0^c	Critical Out of Plane Shear Stress [Nm ⁻²]

rupture pulse with a fast-moving leading tip followed by a second healing tip, trailing at a fixed distance behind the leading tip. Both tips move with the same velocity. This problem belongs to the first type of steady state crack growth problem according to the classification of Freund [4]. The prototype problem of such a crack propagating along a straight path in an isotropic body under uniform loading was proposed and solved by Yoffe [5], while similar pulse-like rupture problems were analyzed by [6,7]. This type of cracks carries great importance in seismology as also noticed by [8] who solved the steady state mode III Yoffe-type crack problem in an elastic strip and calculated the corresponding stress intensity factors and in [9] who made use of a similar finite crack length configuration to model the 2001 M_w 8.1 Kokoxili (Kunlun) Tibet earthquake. Mode III rupture is expected to take place at the extremities of the slipping zone along strike for dip-slip faulting geometries and along the depth of vertical dip-slip faulting as noted by [10].

Strain gradients are very large near the two tips of the finite crack., and thus the flexoelectric effect is also expected to be significant there. In linear elastic solids, stress distributions of semi-infinite mode III cracks were studied by [11] by using a cohesive force model, by [12] in a long strip configuration, and for the finite crack Yoffe-type problem by [13,14]. The Yoffe-type fracture problem has also been analyzed in terms of piezoelectricity by [15–17] while a more general case involving a polarization saturation model was studied by [18].

Yoffe's model is a model to idealize dynamic ruptures of seismic faults. The idea is the following: A weak plane (fault) pre-exists in the $x_2 = 0$ plane (Fig. 1). The two half-spaces are held together with high compressive stresses and the ensuing frictional stresses along the whole bonding plane. Thus, the “rupture” does not mean fracture of initially intact material; instead, the front crack-tip propagates along the fault plane and the trailing crack-tip closes behind.

The present work studies the anti-plane, Yoffe-type, finite fracture length configuration in a flexoelectric material. Flexoelectric ceramics are already in use as sensors and transducers and can experience dynamic loading such as impact which can be detrimental due to the occurrence of fast fracture related to material brittleness. The governing equations are derived from the total energy density, modified as proposed by [19]. The governing equations resemble the ones of couple stress, gradient, or dipolar elasticity, and the results obtained herein can also be specialized to those in such theories [20,21]. A prior body of literature exists, for example in the context of couple stress elasticity, where the asymptotic solution for the static case was studied by [22] and for the dynamic case by [23].

In our work, the classical case – with no flexoelectricity, is first reviewed and investigated further in Section 2. In Section 3 the flexoelectric case is formulated and analyzed. Subsequently, in Section 4 we obtain the asymptotic displacement field near the crack-tip, the dependence of the dynamic stress intensity factor on loading and geometry, the variation of the out of plane displacement along the crack line (crack shearing profile), the strain gradient field, and the dynamic energy release rate. The results are compared with the results of the classical elasto-dynamic case and other related higher gradient theories. We also point to an interesting analogy with the cohesive zone methodology of classical elastodynamics. In Section 5 we solve for the polarization field. In Section 6 we give the main conclusions. In particular, the analytical crack tip asymptotic mechanical and polarization fields allow us to highlight the influence of

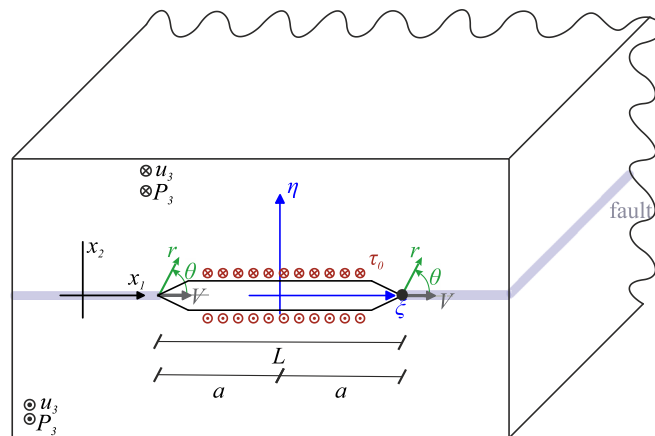


Fig. 1. The anti-plane steady state dynamic problem of a moving mode III Yoffe-type fracture propagating along the x_1 axis with a constant crack tip velocity V , in a flexoelectric material. Constant shear tractions τ_0 , of opposite sign, are prescribed just above and just below the crack faces. The fault pre-exists in the $x_2 = 0$ plane.

the electrical material properties and the presence of a possible strengthening effect. The analysis is complemented with the Finite Element Method (FEM) analysis.

2. General formulation

The steady-state anti-plane (mode III) Yoffe-type crack problem in a flexoelectric material refers to a self-healing mode III finite crack where both crack-tips are propagating with the same steady state velocity. This kind of fracture (or shear pulse) consists of two crack-tips and assumes that the leading one initiates the crack sliding and the trailing one heals it. The displacement along the crack line both in front of the first crack-tip and behind the second one is zero, while it has non-zero values only in the interval between the two traveling crack tips (Fig. 1).

As an anti-plane problem, the mode III Yoffe-type fracture in a flexoelectric material consists of two main unknowns, the out-of-plane displacement $u_3(x_1, x_2, t)$ [m] and the out of plane polarization $P_3(x_1, x_2, t)$ [Cm⁻²], where x_1, x_2 are the in-plane coordinates and t is the time. The energy density function which reduces to eq. (1) as also proposed by [1–3,19,24], with $(\dots)_i = \partial(\dots)/\partial x_i$.

$$U = \frac{1}{2} \left\{ \alpha P_3^2 + (b_{44} + b_{77}) (P_{3,1}^2 + P_{3,2}^2) + 2e_{44} [(\epsilon_{13} + \epsilon_{31})P_{3,1} + (\epsilon_{23} + \epsilon_{32})P_{3,2}] + 2f_{12} [(\epsilon_{13,1} + \epsilon_{31,1})P_3 + (\epsilon_{23,2} + \epsilon_{32,2})P_3] + 2\mu (\epsilon_{13}^2 + \epsilon_{23}^2) \right\} \quad (1)$$

The material constants are the density ρ [kgm⁻³], the atomistic radius a_0 [nm], the shear modulus μ [Nm⁻²], the flexoelectric constant f_{12} [NmC⁻¹], the reciprocal dielectric constant α [Nm²C⁻²], the inverse flexoelectric constant e_{44} [NmC⁻¹], the gradient polarization constant $(b_{44} + b_{77})$ [Nm⁴C⁻²] and P_{max} [Cm⁻²] is the maximum polarization that can be sustained. Properties of three characteristic flexoelectric materials are shown in Table 1. Consider an equivalent microstructural length $\ell/\sqrt{2}$ and an equivalent micro-inertial length $H/\sqrt{12}$ as follows:

$$\frac{\ell^2}{2} = \frac{b_{44} + b_{77}}{\alpha} - \frac{(e_{44} - f_{12})^2}{\mu\alpha} \geq 0 \quad (2)$$

$$\frac{H^2}{12} = \frac{b_{44} + b_{77}}{\alpha} \geq \frac{\ell^2}{2} \quad (3)$$

Note that these lengths are due to the flexoelectric and dielectric material properties. For zero body force and zero initial electric field minimization of the total energy density results into two decoupled equations [21,25], one for the displacement and one for the polarization, according to:

$$\mu \nabla^2 u_3 - \mu \frac{\ell^2}{2} \nabla^4 u_3 = \rho \frac{\partial^2 u_3}{\partial t^2} - \frac{\rho H^2}{12} \nabla^2 \frac{\partial^2 u_3}{\partial t^2} \quad (4)$$

$$P_3 - \frac{\ell^2}{2} \nabla^2 P_3 = \frac{\rho}{\mu} \left(\frac{e_{44} - f_{12}}{\alpha} \right) \frac{\partial^2 u_3}{\partial t^2} \quad (5)$$

Equations (4) and (5) are derived using the minimization of the total energy enthalpy with respect to u_3 and P_3 starting from eq. (1). This results in Euler conditions for all the material points of the body; the conservation of linear momentum, electric field and also Maxwell equation outside and inside the body (for the anti-plane formulation) as shown in [21,25,26].

Both equations (4) and (5) refer to the decoupled flexoelectric problem. A similarity of eq. (4) with couple stress elasticity is easily observed (which has been used in our previous work [1]), and also allows us to consider results from couple stress, and gradient

Table 1

Material constants of SrTiO₃, PMMA, KTaO₃ and KCℓ. The constants have been obtained directly from [21,25,30].

Parameter	Dimension	Material			
		SrTiO ₃	PMMA	KTaO ₃	KCℓ
a_0	nm	0.391	0.415	0.399	0.314
ρ	kg/m ³	5174	7520	6970	1980
$c_{44} = \mu$	GPa	122	110	107	6.8
α	10 ⁸ Nm ² /C ²	2.12	0.168	0.355	243
$b_{44} + b_{77}$	10 ⁻⁹ Nm ⁴ /C ²	2.00	0.115	0.435	1.20
$e_{44} - f_{12}$	Nm/C = V	-10.00	2.00	6.00	-0.215
P_{max}	μC/cm ²	42	57	24	-
c_s	m/s	4856	4583	3910	1853
$H/\sqrt{12}$	nm	3.07	2.62	3.50	0.2222
$\ell/\sqrt{2}$	nm	2.36	2.17	1.66	0.2216
$H/(\ell\sqrt{6})$	-	1.30	1.21	2.11	1.003

elasticity theories [22,23,27]. A short discussion of the decoupled problem and the associate boundary conditions is given in the Appendix.

Stability is assured, if $(b_{44} + b_{77})\mu > (e_{44} - f_{12})^2$ provided that $\alpha > 0$ [28,29]. The material parameters must obey the inequalities suggested in eqs. (2) and (3), in order for the energy density to be positive definite and hence provide uniqueness conditions. Otherwise, the constitutive laws must include other stabilizing terms, e.g., strain gradient effects [1]. Without loss of generality, the two crack-tips are moving with a constant velocity V in the direction of x_1 . We can consider a local moving coordinate system (ξ, η) fixed in the middle of the crack length, where the horizontal axis ξ is parallel to the crack line and the vertical axis η is perpendicular to the crack line, as depicted in Fig. 1. Then we can apply in eqs. (4) and (5), the following coordinate transformation:

$$\xi = x_1 - Vt \tag{6}$$

$$\eta = x_2 \tag{7}$$

This will result into the steady state version of the equations for the displacement and the polarization ($c_s = \sqrt{\mu/\rho}$ is the shear wave velocity):

$$\left(1 - \frac{V^2}{c_s^2}\right) \frac{\partial^2 u_3}{\partial \xi^2} + \frac{\partial^2 u_3}{\partial \eta^2} - \frac{\ell^2}{2} \left(1 - \frac{V^2 H^2}{6\ell^2 c_s^2}\right) \frac{\partial^4 u_3}{\partial \xi^4} - \frac{\ell^2}{2} \left(2 - \frac{V^2 H^2}{6\ell^2 c_s^2}\right) \frac{\partial^4 u_3}{\partial \xi^2 \partial \eta^2} - \frac{\ell^2}{2} \frac{\partial^4 u_3}{\partial \eta^4} = 0 \tag{8}$$

$$P_3 - \frac{\ell^2}{2} \nabla^2 P_3 = \left(\frac{e_{44} - f_{12}}{\alpha}\right) \frac{V^2}{c_s^2} \frac{\partial^2 u_3}{\partial \xi^2} \tag{9}$$

Figure 1 gives a schematic representation of the steady state mode III Yoffe-type fracture growing along its own plane in a flexoelectric material.

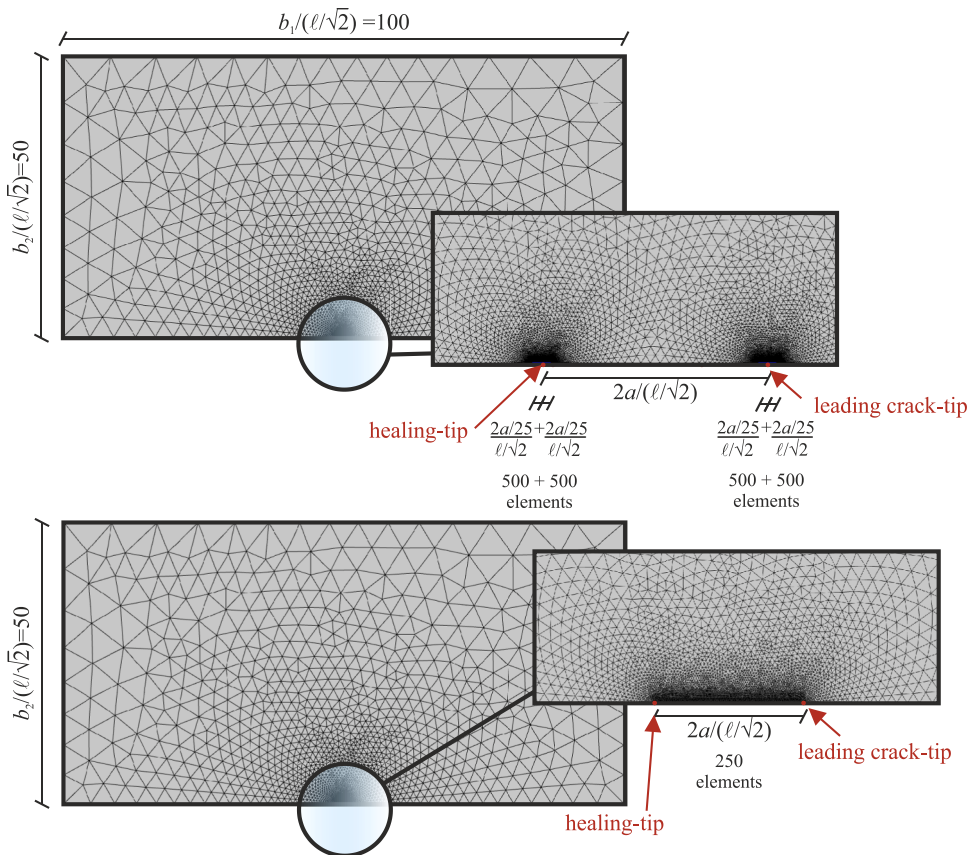


Fig. 2. The Mesh used for the numerical analysis of the anti-plane Yoffe-type problem. Triangular Lagrange type elements of quadratic order were used. The dimensions of the section b_1, b_2 were much larger than the crack length $2a$ ($2a/b_1 = 0.05$). The first mesh provided better resolution near the tips. However, the results with the second mesh converged faster.

3. The classical case

The classical elasto-dynamic case is a subcase of the main Flexoelectric problem formulated in section 2. For this case, we assume vanishing microstructural length $\ell/\sqrt{2} = 0$ and microstructural length ratio $H/(\sqrt{6}\ell) = 1$. Then eq. (8) transforms into eq. (10), which describes the displacement for the classical anti-plane mode III fracture:

$$\left(1 - \frac{V^2}{c_s^2}\right) \frac{\partial^2 u_3}{\partial \xi^2} + \frac{\partial^2 u_3}{\partial \eta^2} = 0 \tag{10}$$

Therefore, the problem is a classical, steady state, anti-plane shear, elastodynamic problem of the type analyzed in [4]. A numerical analysis was performed using the commercial Finite Element / Differences code COMSOL [31]. This code was used to solve both the classical elasticity as well as the flexoelectricity crack problem. Due to the problem’s anti-symmetry, only half of the space was modeled. The FE model approximates a semi-infinite domain (where our theoretical analysis was performed), using a rectangular section with $b_1, b_2 > 2a > \ell/\sqrt{2}$, where b_1, b_2 are the section’s dimensions and $2a$ is the crack length. The crack was located in the middle of the larger size of the section $b_1 > b_2$.

Two different meshes were used, as depicted in Fig. 2. The first mesh consisted of a dense region around each crack-tip; while for the second mesh the elements were distributed uniformly along the crack line. The first mesh used 500 elements in the region of $8 * 10^{-4} b_1 / (\ell/\sqrt{2})$ around each crack-tip, obtaining a model consisting of 52,689 domain elements and 2381 boundary elements. The element size increased with a growth ratio of 1.1 and curvature of 1.1 up to the maximum element size of $10 (\ell/\sqrt{2})$. The second mesh consisted of 14,251 domain and 477 boundary elements, with 250 elements along the crack sliding. The size of the element increased with growth ratio 1.1 and curvature factor 0.3. In all cases the element type was set to be of triangular Lagrange type of quadratic order. The first mesh provided a great number of elements around each tip to assure a greater resolution within that region. The second mesh, despite featuring substantially less elements, provided quite accurate results. Note that regular elements rather than singular ones were used in order not to enforce the singularities of the problem, because the polarization field, and the displacement field may have different crack-tip asymptotics. Since it is possible to solve first the mechanical problem and subsequently the polarization problem, we wanted the mesh to be the same in both problems.

The assumed boundary conditions (B.C.) are shown schematically in Fig. 3. Along the crack line, the boundary conditions were as follows:

$$\begin{aligned} u_3 &= 0 & \text{for } \eta = 0, \xi \leq -a & \quad \text{or} \quad \xi \geq a \\ \frac{\partial u_3}{\partial \eta} &= -\frac{\tau_0}{\mu} & \text{for } \eta = 0, -a \leq \xi \leq a \end{aligned} \tag{11}$$

At the outer boundary (far away from the crack) zero normal derivatives of the displacement were applied in order to approximate the boundary condition at infinity [1], i.e.:

$$\left[n_{x_1} \frac{\partial}{\partial \xi} + n_{x_2} \frac{\partial}{\partial \eta} \right] u_3 = 0 \tag{12}$$

where $\vec{n} = (n_{x_1}, n_{x_2})$ is the normal unit vector at the outer boundary (the shear stress goes to zero at infinity). The shear traction is constant and applied along the crack face (it follows the steady state rupture). Due to the steady state formulation of the problem, the FEM mesh is fixed in the moving coordinate system.

The Finite Element contours of the normalized displacement field at different crack velocities $0 \leq V/c_s < 1$ are given in Fig. 4. We note that increasing V/c_s leads to increasing the displacement magnitude.

The classical problem is subsonic ($V/c_s < 1$) and therefore it is elliptic. The asymptotic crack-tip displacement was investigated by

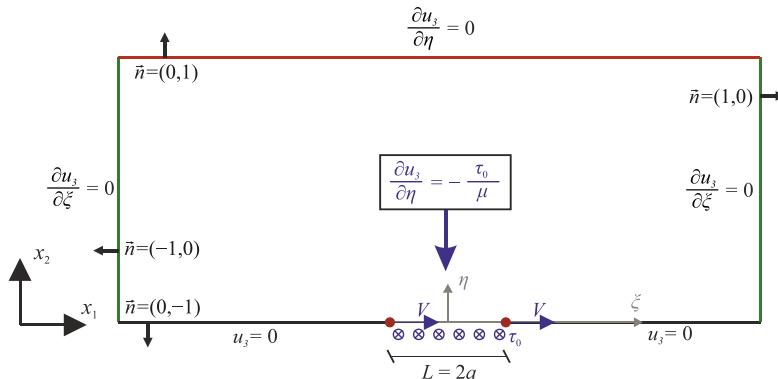


Fig. 3. The implementation of B.C. in the classical mode III Yoffe-type problem.

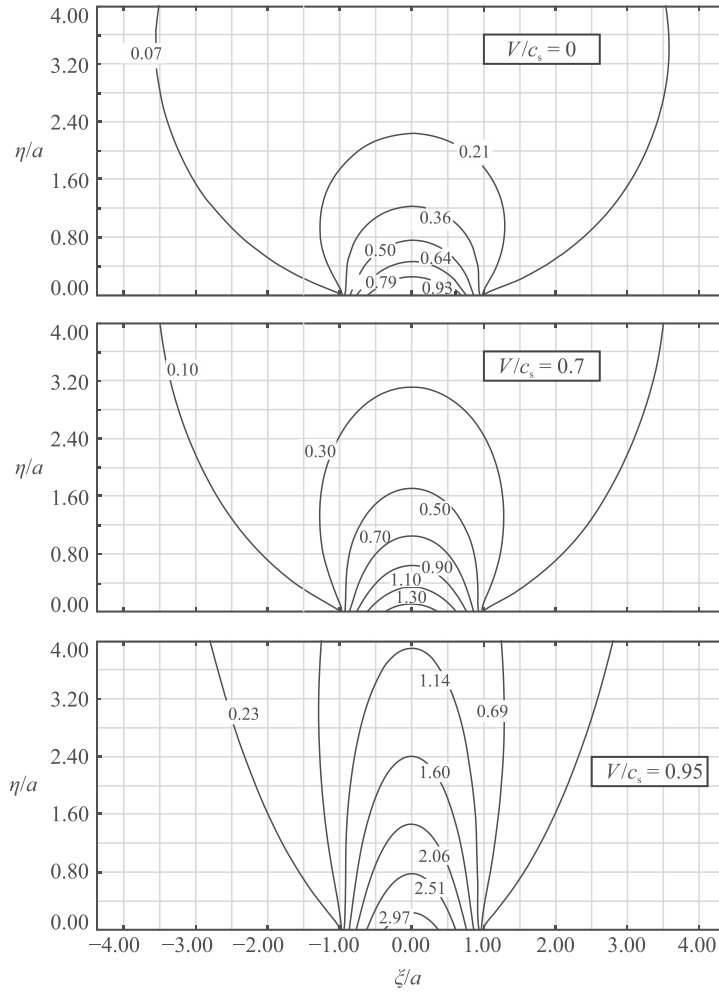


Fig. 4. Contours of the normalized displacement $(u_3\mu)/(a\tau_0)$ in the region near the crack sliding.

Freund [4]. With regard to the healing-tip, the displacement can be given as:

$$u_3 = \frac{2K_{III}r^{1/2}}{\mu\sqrt{2\pi a_s}} \left\{ 1 - \left[\frac{V\sin(\pi - \theta)}{c_s} \right]^2 \right\}^{1/4} \sin \frac{\theta_s}{2} \tag{13}$$

where

$$a_s = \sqrt{1 - \left(\frac{V}{c_s} \right)^2}, \quad \tan\theta_s = a_s \tan(\pi - \theta) \tag{14}$$

The leading crack-tip has asymptotic displacement as in eqs. (13), (14) with θ replaced by $\pi - \theta$. We can re-arrange the near to the tip displacement for the classical case to take the following form.

$$u_3 = B_{classic} r^{1/2} F_{classic}(\theta; V/c_s) \tag{15}$$

From eq. (13) we can see that the angular and the crack tip velocity dependence of the displacement field becomes:

$$F_{classic} = \left[1 - \frac{V^2}{c_s^2} \sin^2(\pi - \theta) \right]^{1/4} \sin \left\{ \frac{\arctan \left[\sqrt{1 - \frac{V^2}{c_s^2}} \tan(\pi - \theta) \right]}{2} \right\} \tag{16}$$

Then by applying (13) and (15), for $\theta = 0$, the amplitude of the asymptotic displacement becomes ($L = 2a$):

$$B_{\text{classic}} = \frac{L^{0.5}}{\sqrt{1 - V^2/c_s^2}} \left(\frac{\tau_0}{\mu} \right) \tag{17}$$

Subsequently this shows that for the classical, mode III Yoffe-type problem we have:

$$K_{III} = B_{\text{classic}} \frac{\mu \sqrt{2\pi}}{2} \sqrt{1 - \frac{V^2}{c_s^2}} = \tau_0 \sqrt{\pi a} = K_{III, \text{static}}^{\text{classic}} \tag{18}$$

This result has also been found by [12,14]. As Fig. 5 demonstrates, the above asymptotic crack-tip displacement holds not only for the leading crack-tip, which initiates the tearing, but also for the trailing one, which completes the healing. In this figure the theoretical displacement proposed by eq. (13) is depicted as solid lines, while the numerical results are depicted as dotted lines.

The energy release rate for the classical mode III Yoffe-type fracture can be given from eq. (19) below and is depicted in Fig. 6 [32].

$$\mathfrak{S} = \frac{K_{III}^2}{2\mu \sqrt{1 - \frac{V^2}{c_s^2}}} = \frac{\tau_0^2 \pi a}{2\mu \sqrt{1 - \frac{V^2}{c_s^2}}} \tag{19}$$

Note that on $V/c_s \rightarrow 1$, $\mathfrak{S} \rightarrow +\infty$. Therefore, the limit velocity is c_s .

If we assume a Griffith type of strength criterion, then $\mathfrak{S} = \mathfrak{S}_c$, where \mathfrak{S}_c is a critical energy release rate thought as a material parameter. The critical loading can be written as:

$$|\tau_0^c| = \left[\frac{\mathfrak{S}_c 2\mu \sqrt{1 - V^2/c_s^2}}{\pi a} \right]^{1/2} \tag{20}$$

Equation (20) implies that as $V/c_s \rightarrow 1$, the critical load τ_0^c required for crack propagation decreases to zero and the rupture is unstable.

On the other hand, we can assume a critical stress intensity factor K_{III}^c , thought as a material parameter. Then, the critical loading in this case is:

$$|\tau_0^c| = \frac{K_{III}^c}{\sqrt{\pi a}} \tag{21}$$

The displacement gradients for the classical case can be estimated with the following equations [13].

$$\sqrt{1 - \frac{V^2}{c_s^2}} \frac{\mu}{\tau_0} \frac{\partial u_3}{\partial \xi} = \text{Im} \left[f \left(\xi + i \sqrt{1 - \frac{V^2}{c_s^2}} \eta \right) \right] \tag{22}$$

$$\frac{\mu}{\tau_0} \frac{\partial u_3}{\partial \eta} = \text{Re} \left[f \left(\xi + i \sqrt{1 - \frac{V^2}{c_s^2}} \eta \right) \right] + 1 \tag{23}$$

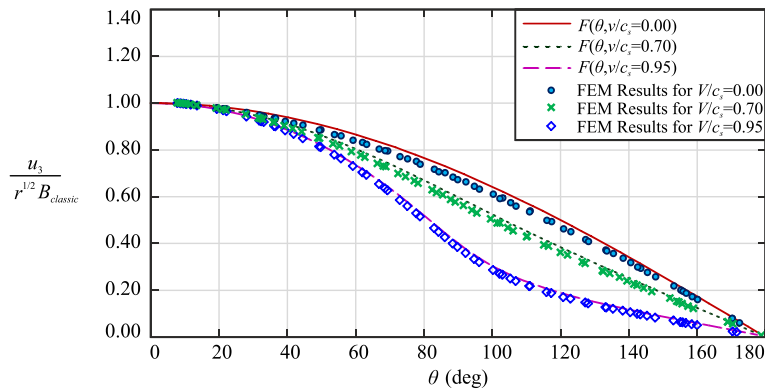


Fig. 5. The normalized asymptotic angular variation around the healing-tip for three velocities and comparison with the theoretical solution and the finite element results. For the leading crack-tip $\theta \rightarrow \pi - \theta$. The region of validity was found to have a length of $(\ell/\sqrt{2})/3$.

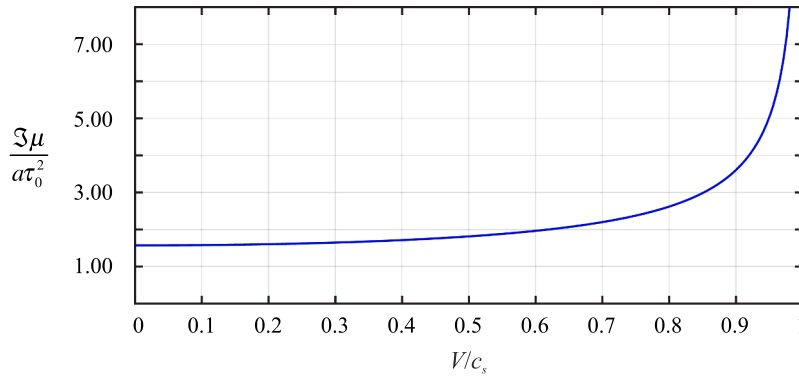


Fig. 6. The energy release rate for the classical elastodynamic case.

$$f\left(\xi + i\sqrt{1 - \frac{V^2}{c_s^2}}\eta\right) = \frac{\frac{\xi}{a} + i\sqrt{1 - \frac{V^2}{c_s^2}}\frac{\eta}{a}}{\left[\left(\frac{\xi}{a} + i\sqrt{1 - \frac{V^2}{c_s^2}}\frac{\eta}{a}\right)^2 - 1\right]^{1/2}} \quad (24)$$

In Fig. 7 the displacement gradients $\partial u_3/\partial \xi$ and $\partial u_3/\partial \eta$ are displayed for different crack-tip propagation velocities. Note that the first ξ -derivative is proportional also to the normalized out of plane velocity $(\partial u_3/\partial t)/V = -\partial u_3/\partial \xi$. The results are shown close to the leading crack-tip and will be compared in section 4 with those of the flexoelectric case.

We further examined the asymptotic nature of the displacement field by considering more terms in the expansion (15). Following [4,33] we obtained:

$$u_3 = B_{\text{classic}} r^{1/2} F_{\text{classic}}(\theta; V/c_s) + \frac{\tau_0}{\mu} r \sin\theta + O(r^{3/2}) \quad (25)$$

The second asymptotic term $O(r)$ has been verified from the FEM results. The region of validity of the asymptotic analysis by keeping two terms extends to $r < a/3$.

In addition, the displacement along the crack line was found analytically by integrating eq. (22):

$$\frac{u_3}{a} \frac{\mu}{\tau_0} = \frac{\left[1 - \left(\frac{\xi}{a}\right)^2\right]^{1/2}}{\sqrt{1 - \frac{V^2}{c_s^2}}} \quad (26)$$

This relation agrees with the FEM results, as Fig. 8 clearly suggests. To summarize, u_3 is symmetrical (Fig. 8), $\partial u_3/\partial \xi$ is anti-symmetrical while $\partial u_3/\partial \eta$ is also symmetrical (Fig. 7).

In conclusion, we have verified the full field and the asymptotic relations of the classical mode III Yoffe problem. We have found two new analytical results in eqs. (25) and (26). Moreover, we showed excellent agreement between the analytical solutions and the FE results in the classical elastodynamic case (also done for the first time).

4. The flexoelectric case

For the flexoelectric case we have:

$$\frac{\rho^2}{2} > 0 \quad \& \quad \frac{H^2}{6\rho^2} > 1 \quad (27)$$

The above inequalities have been discussed in [1] and assure the uniqueness of the solution because the energy density ratio is positive definite. Moreover, the microstructural lengths ratio is $H^2/6\rho^2 > 1$.

As discussed extensively in [1], the regions of ellipticity/hyperbolicity of any steadily growing mode III problem are related to the parameter $\lambda = (V^2/c_s^2)(H^2/6\rho^2)$. Recall that V/c_s is the parameter appearing in the classical case. If $\lambda < 1$ the problem is elliptic, because the displacement eq. (8) is elliptic. If $\lambda = 1$, then the displacement equation and thus the problem is parabolic, and finally, when $\lambda > 1$ the problem is hyperbolic. The categorization of the problem is depicted in Fig. 9, adopted from [21].

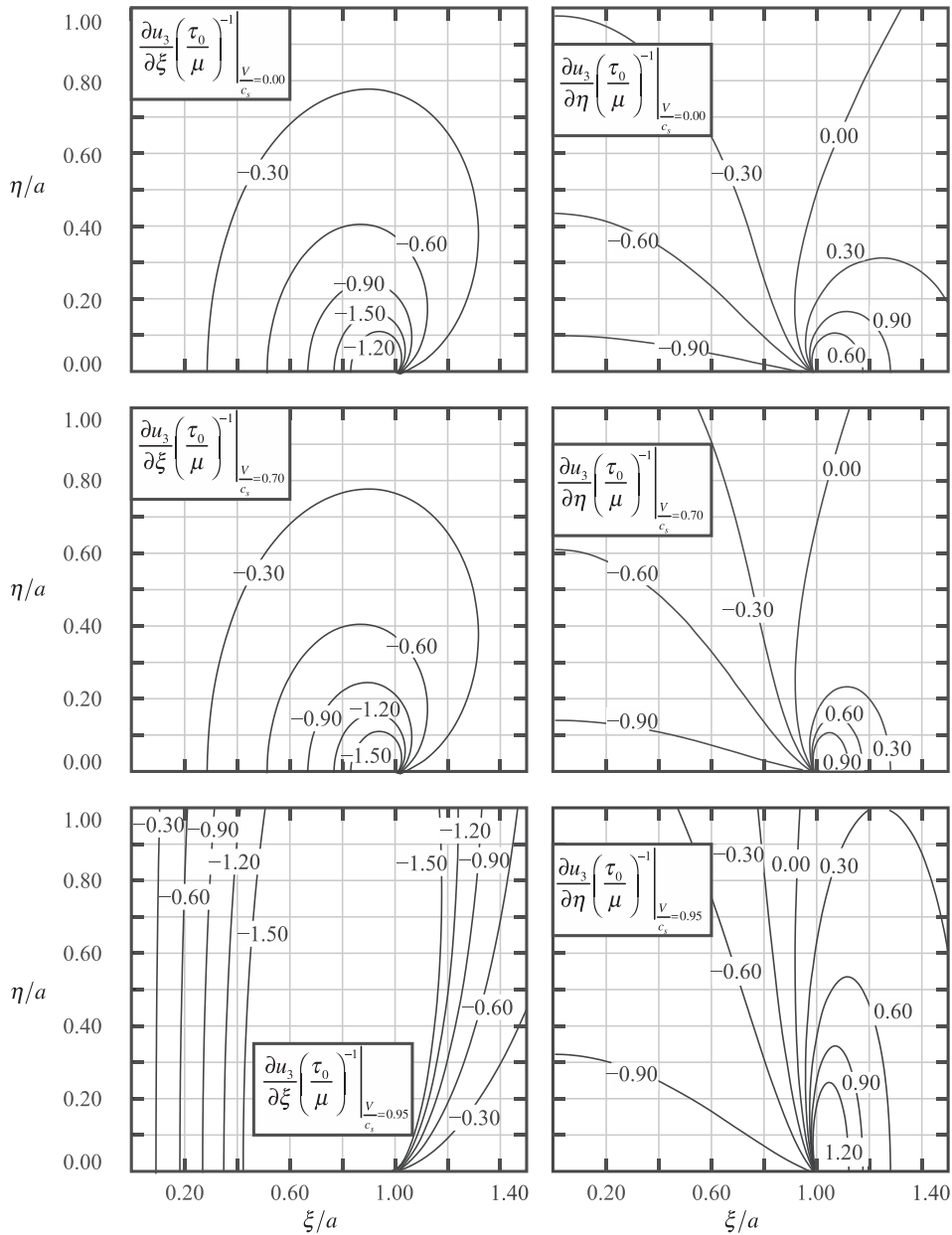


Fig. 7. The normalized derivatives of the displacement with respect to the ξ and η coordinates for, $V/c_s = 0.95, 0.70, 0.00$, using eqs. (22) and (23). Note that the same figure gives the out of plane velocity $(\partial u_3/\partial t)/V = -\partial u_3/\partial \xi$. The results are shown close to the leading crack-tip.

4.1. The elliptic problem

In this section we will deal with the displacement equation for the elliptic problem outlined in Fig. 9 (i.e. when $c_s/V < H/\sqrt{6}l$). A numerical analysis was performed using the finite element code COMSOL described and validated in section 3. For the elliptic case, both meshes proposed in Fig. 2 were used.

The boundary conditions of the problem are discussed in Fig. 10. Along the crack line we have [21]:

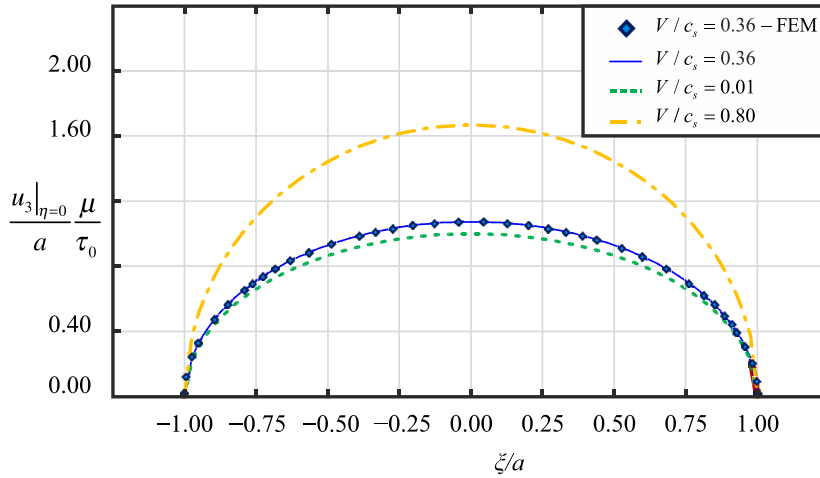


Fig. 8. The normalized displacement along the crack lines for the classical case. This displacement is related only to the velocity of the crack-tips (eq. (26)). Finite Element results are in excellent agreement with eq. (26).

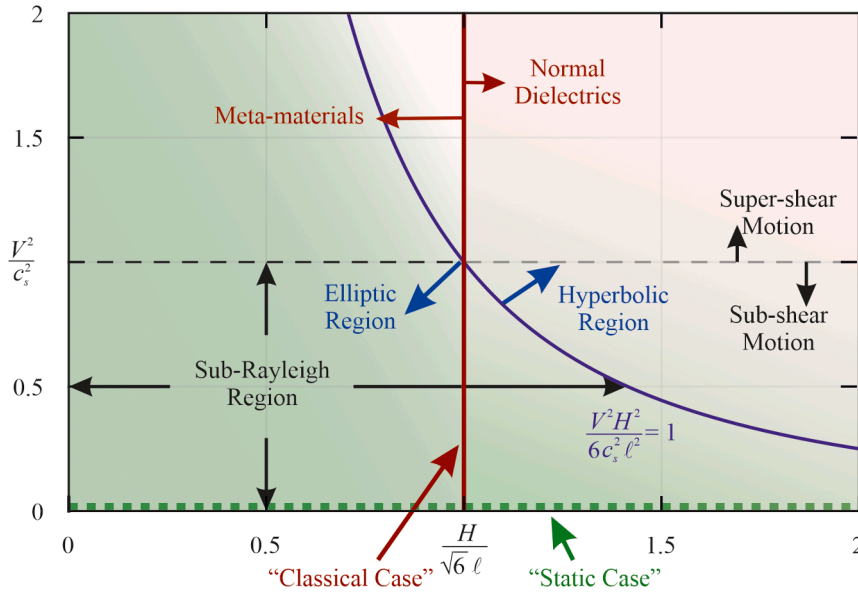


Fig. 9. The three regions that appear in the flexoelectric anti-plane steady state problem, [21]. The elliptic region is bounded by $c_s/V > H/\sqrt{6}\ell$. The hyperbolic region is bounded by $c_s/V < H/\sqrt{6}\ell$. The parabolic region is at $c_s/V = H/\sqrt{6}\ell$.

$$\begin{cases} u_3 = 0 & \text{for } \xi \leq 0 \text{ or } \xi \geq L \\ \frac{\partial u_3}{\partial \eta} - \frac{\ell^2}{2} \left[\left(2 - \frac{H^2}{6\ell^2} \frac{V^2}{c_s^2} \right) \frac{\partial^3 u_3}{\partial \xi^2 \partial \eta} + \frac{\partial^3 u_3}{\partial \eta^3} \right] = -\frac{\tau_0}{\mu} & \text{for } 0 \leq \xi \leq L \\ \frac{\partial^2 u_3}{\partial \eta^2} = 0 & \text{for } \xi \leq 0 \text{ or } \xi \geq L \end{cases} \quad (28)$$

Also, along the crack length ($0 < \xi < L$) the natural condition gives $P_3 = 0$.

These boundary conditions suggest shear stress equal to τ_0 along the crack opening, while everywhere else zero displacement along the crack line, as the classical Yoffe Problem suggest [5].

In order to model the boundary conditions at infinity (absence of shear tractions), we inserted the following conditions at the outer sides of the computational region [21], with $\vec{n} = (n_{x_1}, n_{x_2})$ the normal unit vector to the boundaries of the computational region:

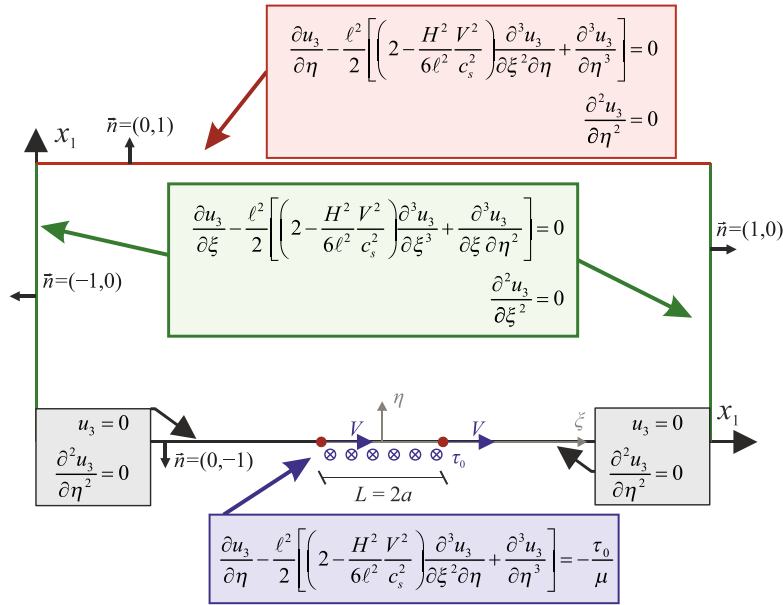


Fig. 10. The boundary conditions of the elliptic mode III anti-plane Yoffe flexoelectric problem for a rectangular computational region.

$$\begin{aligned}
 & \left[n_{x_1} \frac{\partial}{\partial \xi} + n_{x_2} \frac{\partial}{\partial \eta} \right] \left\{ u_3 - \frac{l^2}{2} \left[\left(2 - \frac{H^2 V^2}{6 l^2 c_s^2} \right) \frac{\partial^3 u_3}{\partial \xi^2 \partial \eta} + \frac{\partial^3 u_3}{\partial \eta^3} \right] \right\} = 0 \\
 & n_{x_1} \frac{\partial^2 u_3}{\partial \xi^2} + n_{x_2} \frac{\partial^2 u_3}{\partial \eta^2} = 0
 \end{aligned}
 \tag{29}$$

These boundary conditions suggest zero shear stress and zero moment at infinity. The boundary conditions of the anti-plane mode III flexoelectric problem have been discussed in [25].

In Fig. 11, the computed displacements for three characteristic length scales and velocities are presented. Comparing the results with those of the classical case (Fig. 4) we observe that as the microstructural length $l/\sqrt{2}$ increases, the displacements decrease. Therefore, a stiffening effect is revealed due to the presence of this microstructural length that relates to flexoelectric material constants (see eq. (2)).

The asymptotic crack-tip displacement can be calculated using eq. (8), keeping only the higher order derivative terms. Then eq. (8) is reduced to:

$$\nabla^4 u_3 - \lambda \nabla^2 u_{3,\xi\xi} \approx 0
 \tag{30}$$

where $\lambda = (H^2 V^2)/(6 l^2 c_s^2) > 0$. The problem resembles that of couple stress elasticity [23] and so we can consider a displacement near to the crack-tip of the form:

$$u_3(r \rightarrow 0, \theta; \lambda) = r f(\theta; \lambda) + r^{3/2} F(\theta; \lambda) + O(r^{5/2})
 \tag{31}$$

The term of order $O(r^{3/2})$, is the only one that will provide a positive energy release rate in the flexoelectric case. However, the FEM results show that the asymptotic displacement is also influenced by a term of order $O(r)$. We can deal with each term of different order separately and we first consider the term $O(r)$:

$$u_3 = r f(\theta; \lambda)
 \tag{32}$$

When eq. (32) is substituted in to eq. (30) it becomes:

$$\begin{aligned}
 & f(\theta; \lambda) [-12\lambda \cos^2(\theta) + 4\lambda + 4] + f'(\theta; \lambda) [-16\lambda \sin(\theta) \cos(\theta)] + f''(\theta; \lambda) [-8\lambda \cos^2(\theta) \\
 & + 8] + f'''(\theta; \lambda) [-16\lambda \sin(\theta) \cos(\theta)] + f^{IV}(\theta; \lambda) [4\lambda \cos^2(\theta) - 4\lambda + 4] = 0
 \end{aligned}
 \tag{33}$$

The latin superscripts denote the order of the derivative with respect to θ . Equation (33) has the following general solution:

$$f(\theta; \lambda) = \kappa_1 \cos(\theta) + \kappa_2 \sin(\theta) + \kappa_3 \frac{1}{\sqrt{\cos(2\theta) + \sin(2\theta)i}} + \kappa_4 \sqrt{\cos(2\theta) + \sin(2\theta)i}
 \tag{34}$$

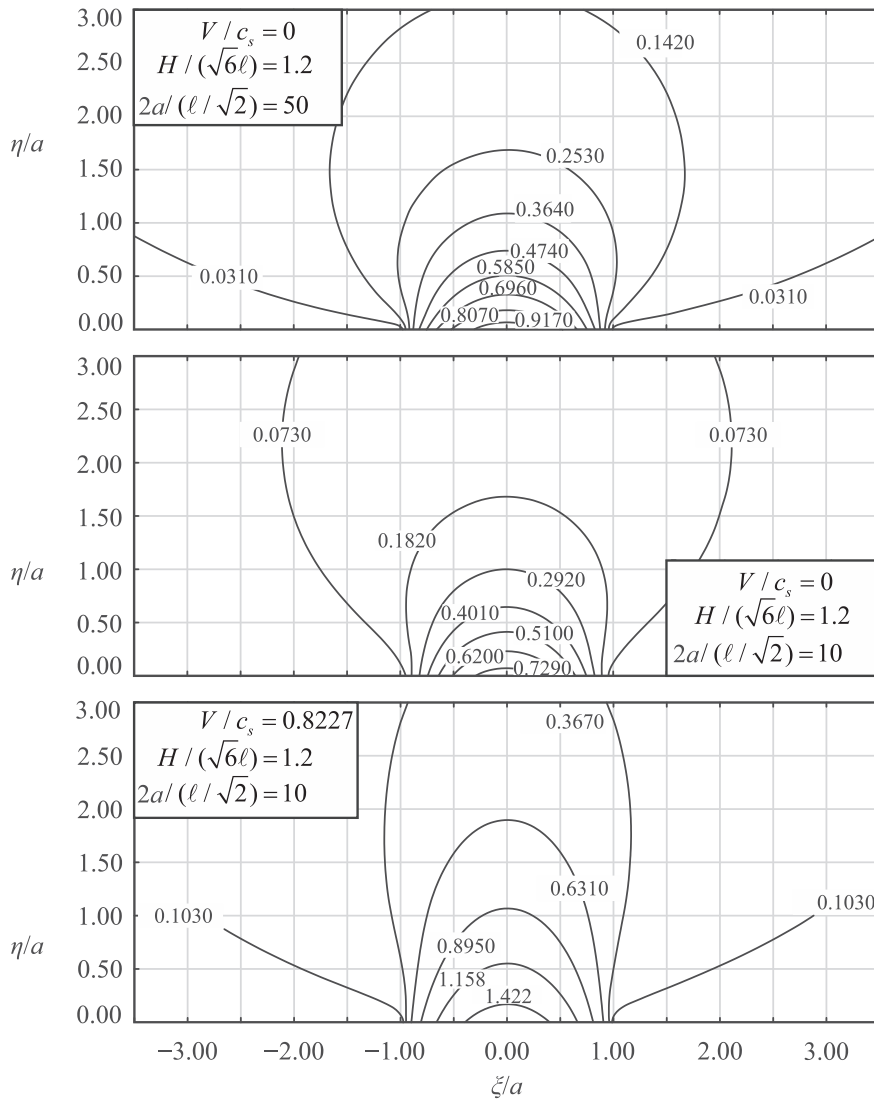


Fig. 11. The normalized displacement ($u_3\mu$)/($a\tau_0$) field in a region near the crack sliding for three flexoelectric cases as computed from the FEM analysis.

where $i = \sqrt{-1}$, κ_1, κ_2 are real constants and κ_3, κ_4 are complex constants so that $f(\theta, \lambda)$ be real. All constants depend on λ , the loading and the material constants as will show later in eq. (37). The boundary conditions that eq. (28) suggests are transformed using polar coordinates, keeping only the higher order terms, as the asymptotic analysis demands [30]. Taking into consideration the anti-symmetry of the mode-III problem $f(-\theta) = -f(\theta)$, we obtain: $\kappa_1, \kappa_3, \kappa_4 = 0$ with $\kappa_2 = b \neq 0$.

Including the asymptotic term $O(r)$, the near-tip displacement approximation becomes:

$$u_3(r \rightarrow 0, \theta; \lambda) = br \sin(\theta) + r^{3/2} F(\theta; \lambda) \tag{35}$$

For the elliptic case we have found $F(\theta; \lambda)$ in [30], and for the healing-tip is:

$$F(\theta; \lambda) = B \frac{3\sqrt{2}}{4(\lambda - 4)} \times \left\{ \frac{4(\lambda - 1)}{3\lambda} \left[(2\cos\theta + 1)\sqrt{1 - \cos\theta} + (\lambda - 2) \left(\cos\theta - \frac{1}{2} \right) \sqrt{1 + \cos\theta} \right] - \frac{2(\lambda - 4)}{3\lambda} \cos \left[\left(\frac{3}{2} \right) \arcsin \left(\frac{\cos\theta}{\sqrt{\lambda \cos^2\theta - \lambda + 1}} \right) \right] (\lambda \cos^2\theta - \lambda + 1)^{3/4} - \sqrt{2\sqrt{\lambda \cos^2\theta - \lambda + 1} + 2\sin\theta\sqrt{1 - \lambda} \cos\theta} \right\} \tag{36}$$

For the leading crack-tip, eq. (36) holds with $\theta \rightarrow \pi - \theta$. The estimation of the two amplitudes b and B can be done using FEM results. For $\theta = 0$, we can estimate for different combinations of $\ell/\sqrt{2}$, $2a/(\ell/\sqrt{2})$, λ , $H/\sqrt{6\ell}$ the amplitude B , because $f(\theta = 0) = 0$. For $\theta = \theta_r$, that makes $F(\theta_r) = 0$, we can estimate the amplitude b . In Fig. 12 the angle θ_r is depicted for different values of $\lambda \in (0, 1)$.

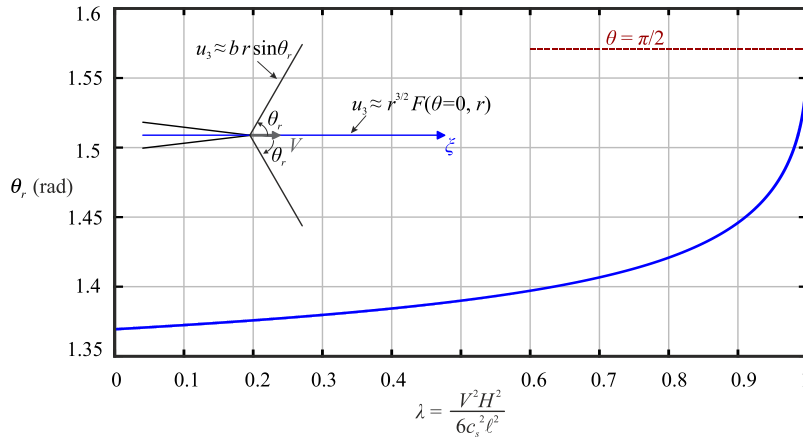


Fig. 12. The root of eq. (36), $F(\theta = \theta_r) = 0$ for the leading crack tip (for the healing-tip we should substitute θ with $\pi - \theta$). For $\theta = \theta_r$ we can estimate the parameter b using the FEM results.

Using this methodology and the FEM results, we ended up with the approximations:

$$\begin{aligned}
 u_3|_{\xi = a} &= 0.35(a)^{3/2} \frac{(\tau_0/\mu)}{(1-\lambda)^{1/4}} \left(\frac{H}{\sqrt{12}}\right)^{-1/2} \left(1 - e^{-\frac{2a}{3\ell}}\right) \\
 \eta &= 0 \\
 B &= 0.75(a)^{1/2} \frac{(\tau_0/\mu)}{(1-\lambda)^{1/4}} \left(\frac{H}{\sqrt{12}}\right)^{-1} \left(1 - e^{-\frac{2a}{3\ell}}\right) \\
 b &= 0.11(a)^{1/2} \frac{\tau_0}{\mu} \left(\frac{H}{\sqrt{12}}\right)^{-1} \left(1 - e^{-\frac{2a}{3\ell}}\right)
 \end{aligned} \tag{37}$$

In Fig. 13 we plotted the normalized near-tip angular variation $F(\theta; \lambda)$ for three different values of λ regarding the healing-tip. The agreement with the FEM is excellent.

Following [30] only the term $O(r^{3/2})$ will result in a positive Energy Release Rate. Using the asymptotic variation $F(\theta)$ and substituting it into the integral presented there (eq. (37) of ref [30]), we can obtain numerically Fig. 14. Figure 14 is a master curve for all elliptic anti-plane dynamic fracture problems.

The Energy Release Rate can be subsequently calculated using the amplitude estimation of B from FEM fitted by eq. (37), according to $\mathfrak{S} = QB^2\mu\ell^2$, as follows:

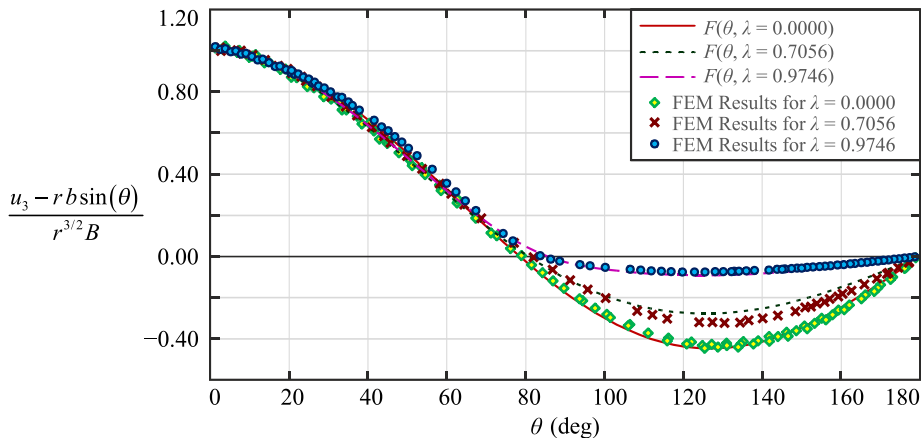


Fig. 13. The angular variation around the crack-tip for three flexoelectric cases and the comparison between the theoretic solution and the finite element results, for the healing-tip that initiates the healing. The region of validity has a length of $(\ell/\sqrt{2})/3$, however further from the crack-tip up to a distance of $\ell/\sqrt{2}$ the influence of the single term of order $O(r^{3/2})$ is major. For the leading crack-tip $\theta \rightarrow \pi - \theta$. Note that for $\lambda \rightarrow 0$ we obtain in the limit the static curve.

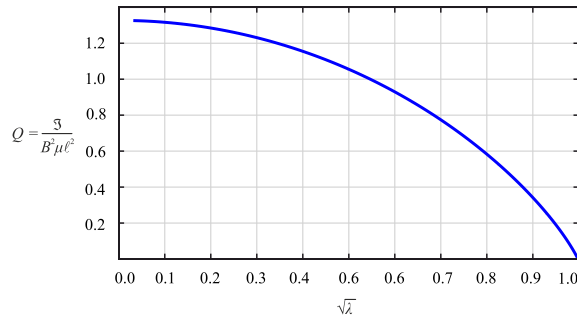


Fig. 14. The normalized energy release rate as it can be calculated using the near-tip $r^{3/2}$ angular variation. This figure is obtained from [30].

$$\frac{\mathfrak{S}\mu}{\tau_0^2 a} = 1.125 \frac{Q}{\sqrt{1-\lambda}} \left(\frac{H}{\sqrt{6}\ell}\right)^{-2} \left(1 - e^{-\frac{2a}{3\ell}}\right)^2 \tag{38}$$

The normalized energy release rate with respect to the parameter λ is presented in Fig. 15. Note the strengthening effect of the microstructure length $\ell/\sqrt{2}$ (increasing $\ell/\sqrt{2}$ leads to decreasing \mathfrak{S}).

The static energy release rate can be given approximately as:

$$\mathfrak{S}_{static} \approx \mathfrak{S}_{classic.static} \left(1 - e^{-\frac{2a}{3\ell}}\right) = \frac{\tau_0^2 \pi a}{2\mu} \left(1 - e^{-\frac{2a}{3\ell}}\right) \tag{39}$$

Consequently, the energy release rate normalized with its static value can be calculated as follows:

$$\frac{\mathfrak{S}}{\mathfrak{S}_{static}} = Q \frac{4B^2}{\pi} \left(\frac{\tau_0}{\mu}\right)^{-2} \frac{\ell^2/2}{a} \left(1 - e^{-\frac{2a}{3\ell}}\right)^{-1} \tag{40}$$

Note that this equation needs the amplitude of the asymptotic solution B . We can use the semi-analytical estimation of B , eq. (37), to form eq. (41), which is the semi-analytical energy release rate normalized by the static value.

$$\frac{\mathfrak{S}}{\mathfrak{S}_{static}} = \frac{2.25}{\pi} \frac{Q}{\sqrt{1-\lambda}} \left(\frac{H}{\sqrt{6}\ell}\right)^{-2} \left(1 - e^{-\frac{2a}{3\ell}}\right) \tag{41}$$

In Fig. 16, the normalized energy release rate given by eq. (41) is depicted for three characteristic cases, while the corresponding FEM results agree well with the theoretical curves for the same cases. Note the difference with the classical case, depicted in Fig. 6, where the J-integral increases monotonically with rupture velocity. In this case, the energy release rate decreases monotonically with rupture speed, therefore a critical \mathfrak{S} leads to a stable steady state rupture speed. A similar result has been found by Rice et al [7] in the context of classical dynamic rupture with a cohesive zone (see section 4.2. for the analogy of the two problems).

The strain in the tangential to the radius direction for the elliptic case is given as:

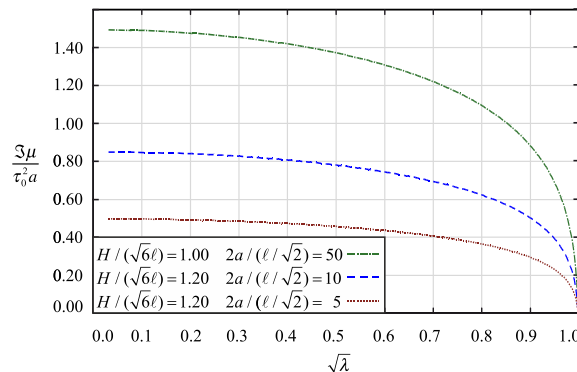


Fig. 15. The normalized energy release rate for different values of $2a/(\ell/\sqrt{2})$.

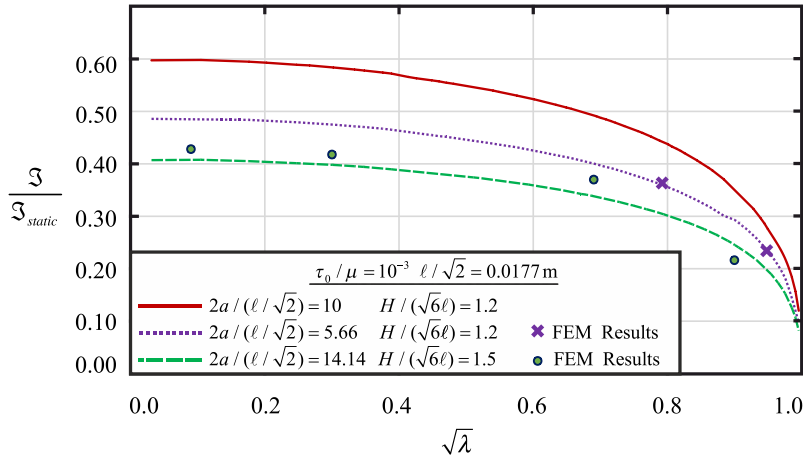


Fig. 16. The normalized energy release rate with respect to its static value.

$$\epsilon_{\theta z} = \frac{1}{2} \frac{1}{r} \frac{\partial u_z}{\partial \theta} = \frac{1}{2} b \cos \theta + \frac{1}{2} r^{1/2} F^{(\theta)} \tag{42}$$

The normalized outer strain ($r^{1/2}$ order) is shown in Fig. 17 for various velocities. Note that the extreme value of the strain at the crack-tip is bounded and appears at $\theta = 0$ and at $\theta = \pi$, giving $\max|\epsilon_{\theta z}| = b/2$. We can use this strain as a strength criterion, assuming it reaches a critical value $\epsilon_{\theta z}^c$:

$$\epsilon_{\theta z}^c = \max|\epsilon_{\theta z}| = \frac{0.11}{2} a \frac{\tau_0}{\mu} \left(\frac{H}{\sqrt{12}} \right)^{-1} \left(1 - e^{-\frac{2a}{3r}} \right) \tag{43}$$

Note again the strengthening effect of the microstructural length $l/\sqrt{2}$. From Fig. 17 we observe that the maximum off-fault shear strain appears around $\theta = \pm 56^\circ$. This is in contrast to the classical case that predicts $\theta = 0^\circ$ for $V/c_s < 0.7$ and $\theta = \pm 90^\circ$ for $V/c_s > 0.7$ [10].

The displacement gradients were obtained from FEM. In Fig. 18 the displacement gradients for three flexoelectric cases are displayed (for the leading crack tip). Note that for $2a/(l/\sqrt{2}) = 50$ there is a similarity with the classical case displayed in Fig. 7 far from the crack-tip. The displacement gradient $\partial u_3/\partial \xi$ also gives the normalized out of plane velocity $-(\partial u_3/\partial t)/V$.

The normalized displacement along the crack line is limited from below for cases with large microstructure ($l > L/2$) and from above for cases with insignificant microstructure $l \ll L/2$ as in the classical case. For the low bound we have eq. (44), while the almost classical case (upper bound) with small microstructure is described by eq. (45). These are elastodynamics limits and are

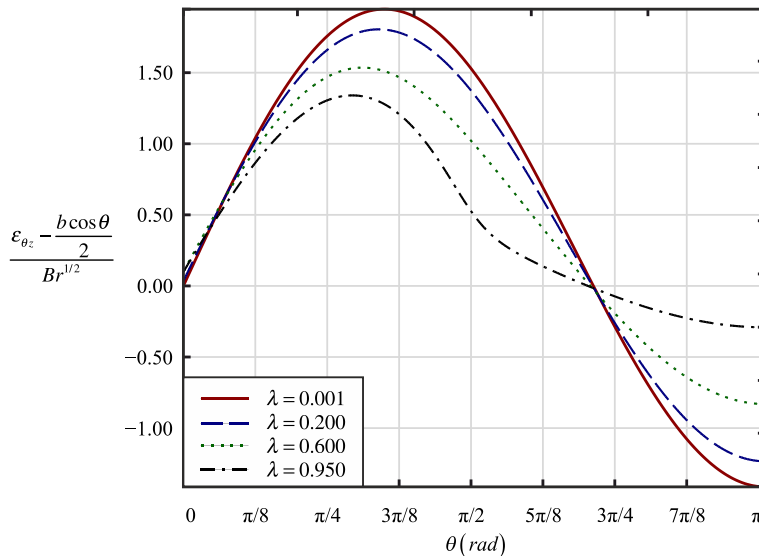


Fig. 17. The normalized outer strain $\epsilon_{\theta z}$ of order $O(r^{1/2})$.

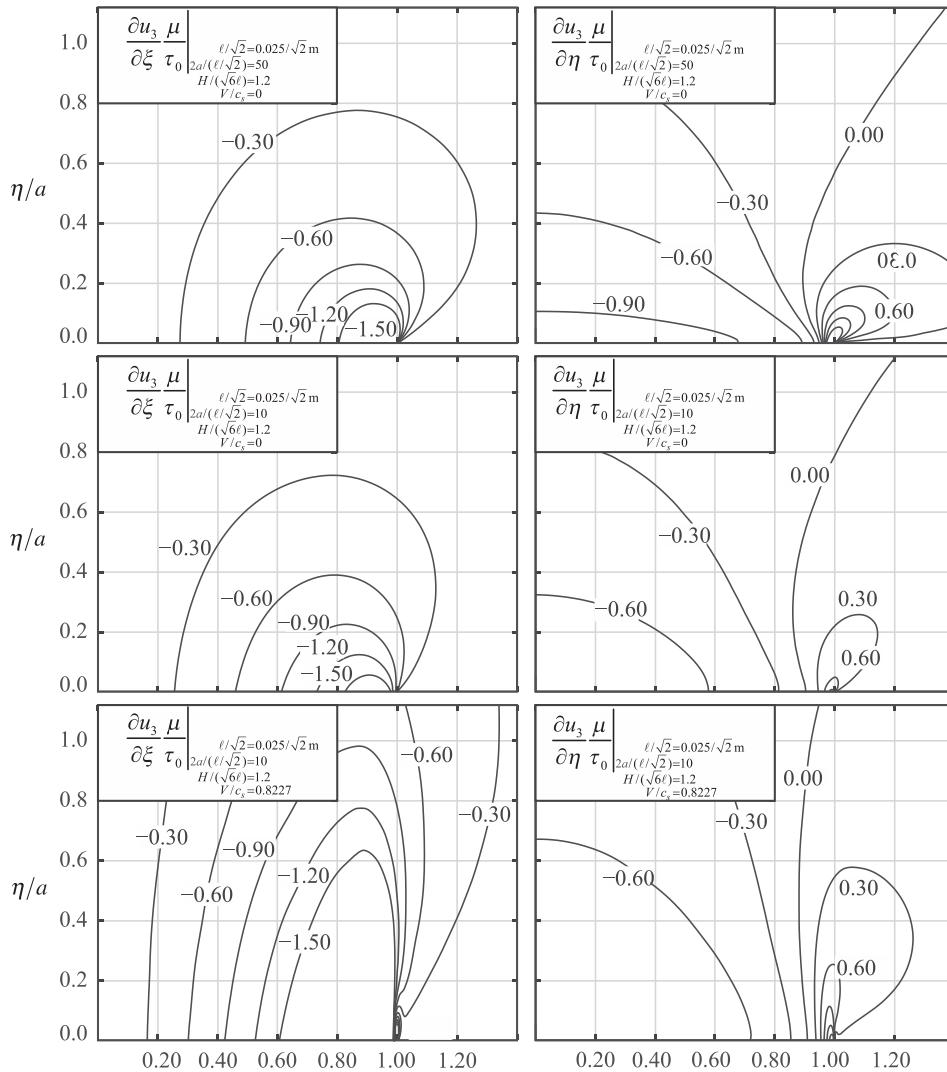


Fig. 18. The displacement gradients for three flexoelectric cases according to FEM results near the leading crack-tip.

presented for the first time.

$$\frac{u_3}{a} \frac{\mu}{\tau_0} = \frac{1}{36} \left(\frac{2a}{\ell/\sqrt{2}} \right)^2 \frac{1}{\left(1 - \frac{V^2}{c_s^2} \frac{H^2}{6\ell^2} \right)^{1/4}} \left[1 - \left(\frac{\xi}{a} \right)^2 \right]^{3/2}, \quad \frac{\ell/\sqrt{2}}{2a} \rightarrow \infty \tag{44}$$

$$\frac{u_3}{a} \frac{\mu}{\tau_0} = \frac{\left[1 - \left(\frac{\xi}{a} \right)^2 \right]^{1/2}}{\left(1 - \frac{V^2}{c_s^2} \right)^{1/4}}, \quad \frac{\ell/\sqrt{2}}{2a} \rightarrow 0 \tag{45}$$

In Fig. 19 the normalized displacement along the crack line is displayed for various cases. Additional results show that the propagation velocity V/c_s and the microstructural length ratio $H/(\sqrt{6}\ell)$, affect only the displacement magnitude and not the displacement distribution along the crack line. This was also observed by [20] for the static problem.

In Fig. 20 we show the normalized maximum displacement which occurs for $\xi = 0$, indicating the stiffening effect due to the increase of the microstructural length.

Regarding the hyperbolic regime, it was found that the Yoffe-type fracture has no solution, just as it is for the classical Yoffe-type problem. We can then conclude that the current problem holds only for $(H^2V^2)/(6\ell^2c_s^2) < 1$ and thus it is always elliptic.

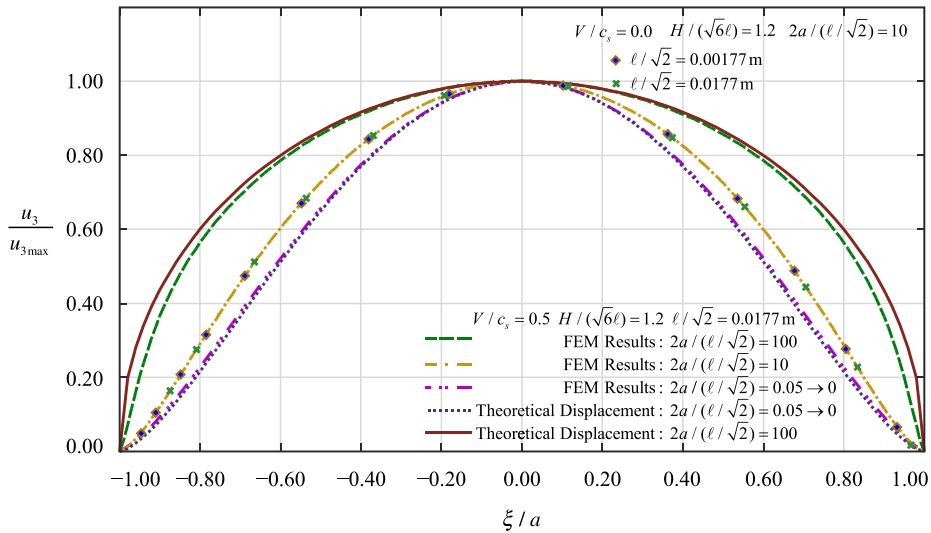


Fig. 19. The normalized displacement along the crack line for the flexoelectric case.

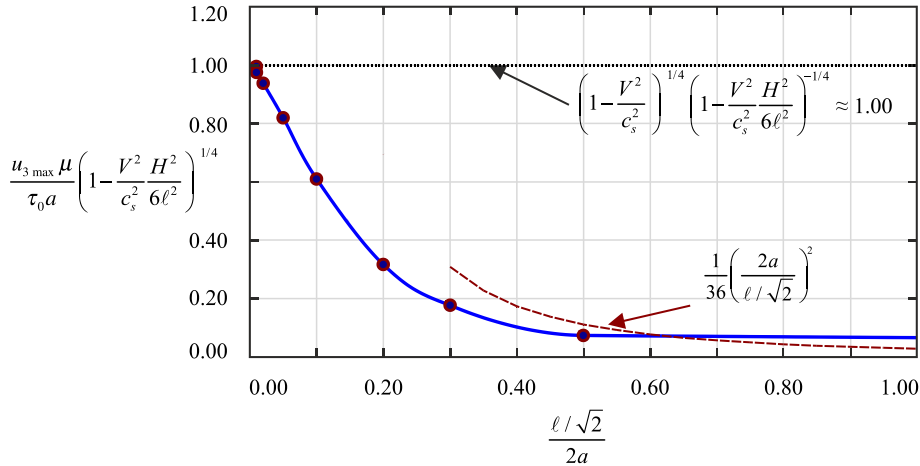


Fig. 20. The normalized maximum displacement obtained from FEM results.

4.2. Analogy with the cohesive zone model

Classical singular crack models assume that the inelastic process is confined very close to the rupture tip. The non-singular slip weakening model introduced by [11,34] in analogy to the cohesive tensile models of Barenblatt – Dugdale type, expand the region of the inelastic process (which is the crack-tip point in classical elastodynamic fracture mechanics). Andrews [35] utilized a slip weakening type of cohesive model for an anti-plane Kostrov-type of crack rupture. Ida [11] suggested a cohesive stress across a fault plane in order to understand the physical mechanism of rupture at the tip of a mode III shear crack, assuming classical elastodynamics. Following his results, we consider a constant cohesive stress σ_0 close to the crack-tip and a classical far-field loading (in our notation). Let the displacement outside the cohesive zone be approximated by (as Ida [11] proposed, assuming small scale cohesive zone where the cohesive length is fully enclosed by the linear elastic asymptotic solution):

$$u_3(\theta = 0, r) \approx B_{\text{classic}} r^{1/2} \tag{46}$$

The far-field J-integral can be found following Ida [11] as:

$$\mathfrak{S}_{\text{classic}} = \frac{\pi \mu B_{\text{classic}}^2}{4} \left[1 - \left(\frac{V}{c_s} \right)^2 \right]^{1/2} \tag{47}$$

For the present problem B_{classic} is given by eq. (17).

The near-tip field, according to Ida [11], follows a $r^{3/2}$ cusp-like crack sliding displacement. This result is in good accord with our finding. Furthermore, Ida found the length of the cohesive zone (R) as:

$$R = \frac{4\mathfrak{N}_{classic}^2}{\sigma_0^2} \ll a \quad (48)$$

Following Ida [11] we can estimate the near-tip displacement as:

$$u_3 \approx -\frac{B_{classic}}{3R} r^{3/2} \quad (49)$$

Now, we can establish an analogy with our results as follows. Let:

$$R \approx 0.63 \frac{(1-\lambda)^{1/4}}{\sqrt{1-V^2/c_s^2}} \left(\frac{H}{\sqrt{12}} \right) \left(1 - e^{-\frac{2a}{3\ell}} \right)^{-1} \quad (50)$$

From (48) we obtain:

$$\sigma_0 = \frac{2\mathfrak{N}_{classic}}{\sqrt{R}} \quad (51)$$

5. The polarization field

In the elliptic mode III problem, the non-homogeneous term in eq. (9) is non-zero. Consider now that eq. (9) refers to a near to the tip region, where the displacement is equal to the asymptotic displacement and so the non-homogeneous term of eq. (9) is equal to

$$V^2 \frac{\partial^2}{\partial \xi^2} u_3 = V^2 \frac{\partial^2}{\partial \xi^2} [A_1(\theta)r + A_2(\theta)r^{3/2}] \quad (52)$$

We can then rewrite eq. (9) as

$$\frac{\ell^2}{2} \nabla^2 P_3 = -\frac{V^2}{c_s^2} \left(\frac{e_{44} - f_{12}}{\alpha} \right) \left[\frac{A_1''}{r} \sin^2 \theta + \frac{A_1'}{r} \sin^2 \theta + \frac{3}{4} \frac{A_2}{r^{1/2}} \cos^2 \theta + \frac{A_2''}{r^{1/2}} \sin^2 \theta - \frac{A_2'}{r^{1/2}} \sin \theta \cos \theta + \frac{3}{2} \frac{A_2}{r^{1/2}} \sin^2 \theta \right] \quad (53)$$

keeping only the higher order derivative terms. Assuming that the polarization is also of the form

$$P_3 = rB_1(\theta) + r^{3/2}B_2(\theta) \quad (54)$$

we end up with a system of two differential equations, one for B_1 and one for B_2 :

$$B_1 + B_1'' = C [A_1'' \sin^2 \theta + A_1' \sin^2 \theta] \quad (55)$$

$$\frac{9}{4} B_2 + B_2'' = C \left[A_2 \left(\frac{3}{4} \cos^2 \theta + \frac{3}{2} \sin^2 \theta \right) - A_2' \sin \theta \cos \theta + A_2'' \sin^2 \theta \right] \quad (56)$$

where $(...)' = d(...)/d\theta$, $(...)^{\prime\prime} = d^2(...)/d\theta^2$ and

$$C = -\frac{V^2}{c_s^2} \left(\frac{e_{44} - f_{12}}{\alpha} \right) \left(\frac{\ell^2}{2} \right)^{-1} \quad (57)$$

Note that the system of differential equations (55) and (56), holds for any anti-plane fracture problem. For the mode III Yoffe-type problem in a flexoelectric material, we have:

$$\begin{aligned} A_1(\theta) &= b \sin(\theta) \\ A_2(\theta; \lambda) &= F(\theta; \lambda) \end{aligned} \quad (58)$$

Then, eq. (55) becomes:

$$B_1 + B_1'' = 0 \quad (59)$$

which has a solution of the form:

$$B_1 = B_1(\theta) = \kappa_5 \sin \theta + \kappa_6 \cos \theta \quad (60)$$

with κ_5, κ_6 real integration constants. Also eq. (56) becomes:

$$\frac{9}{4}B_2 + B_2'' = C \left[F \left(\frac{3}{4} \cos^2 \theta + \frac{3}{2} \sin^2 \theta \right) - F' \sin \theta \cos \theta + F'' \sin^2 \theta \right] \tag{61}$$

The general solution of this differential equation is:

$$B_2 = B_2(\theta) = \kappa_7 \cos \frac{3\theta}{2} + \kappa_8 \sin \frac{3\theta}{2} - \frac{C}{6} \sin \frac{3\theta}{2} \tilde{A} + \frac{C}{6} \cos \frac{3\theta}{2} \tilde{B} \tag{62}$$

Where κ_7 and κ_8 are real constants and $\tilde{A} = \tilde{A}(\theta; \lambda)$, $\tilde{B} = \tilde{B}(\theta; \lambda)$ are the following integrals.

$$\begin{aligned} \tilde{A}(\theta; \lambda) &= \int \cos \frac{3\theta}{2} \left[-3(\sin^2 \theta + 1)F + (4\sin \theta \cos \theta)F' - (4\sin^2 \theta)F'' \right] d\theta \\ \tilde{B}(\theta; \lambda) &= \int \sin \frac{3\theta}{2} \left[-3(\sin^2 \theta + 1)F + (4\sin \theta \cos \theta)F' - (4\sin^2 \theta)F'' \right] d\theta \end{aligned} \tag{63}$$

Therefore, the two terms asymptotic approximation of the polarizations is:

$$P_3 = r(\kappa_5 \sin \theta + \kappa_6 \cos \theta) + r^{\frac{3}{2}} \left[\kappa_7 \cos \frac{3\theta}{2} + \kappa_8 \sin \frac{3\theta}{2} - \frac{\tilde{C}}{6} \sin \frac{3\theta}{2} + \frac{C}{6} \tilde{B} \cos \frac{3\theta}{2} \right] \tag{64}$$

We used boundary conditions around the crack-tips as shown in Fig. 21. Around each crack-tip, we demand zero polarization along the crack line, given by eqs. (65) and (66). These boundary conditions imply Faraday’s cage – like conditions, where at the outer boundary and along the crack, polarization cannot exist.

$$P(\theta = 0) = 0 \Rightarrow \begin{cases} \kappa_6 = 0 \\ \kappa_7 = -\frac{C}{6} (\tilde{B}) \Big|_{\theta=0} \end{cases} \tag{65}$$

$$P(\theta = \pi) = 0 \Rightarrow \begin{cases} \kappa_6 = 0 \\ \kappa_8 = \frac{C}{6} (\tilde{A}) \Big|_{\theta=\pi} \end{cases} \tag{66}$$

And only $\kappa_5 = \kappa \neq 0$.

For the B.C. given by eqs. (65) and (66), the polarization is approximated as:

$$\begin{aligned} P_3 &= r\kappa \sin \theta + \frac{C}{6} r^{\frac{3}{2}} \left\{ \sin \frac{3\theta}{2} \left[(\tilde{A}) \Big|_{\theta=\pi} - (\tilde{A}) \right] - \cos \frac{3\theta}{2} \left[(\tilde{B}) \Big|_{\theta=0} - (\tilde{B}) \right] \right\} \\ &= r\kappa \sin \theta + C\Lambda r^{\frac{3}{2}} \end{aligned} \tag{67}$$

The integrals $\tilde{A}(\theta; \lambda)$ and $\tilde{B}(\theta; \lambda)$ are difficult to evaluate in closed form, so we can use a 7th order Taylor approximation of the function F around $\pi/2$ to simplify the calculations. We found numerically that, as λ increases, the accuracy of the Taylor approximation decreases and that the quantity Λ remains almost invariant for $\lambda < 0.5$

$$\Lambda = \frac{1}{6} \left\{ \sin \frac{3\theta}{2} \left[(\tilde{A}) \Big|_{\theta=\pi} - (\tilde{A}) \right] - \cos \frac{3\theta}{2} \left[(\tilde{B}) \Big|_{\theta=0} - (\tilde{B}) \right] \right\} \tag{68}$$

We calculated the polarization field, using the finite element code COMSOL with the same model used for the calculation of the displacement field. The polarization asymptotic terms (eq. (54)) around the healing-tip are depicted in Fig. 22 (for the leading crack-tip $\theta \rightarrow \pi - \theta$). The overall polarization field is depicted in Fig. 23 and Fig. 24. The numerical results confirmed that the term of order $O(r)$ is the most singular term.

It can be observed that the maximum polarization occurs for $\pi/2$, at a distance $r = \ell/\sqrt{2}$ from the crack-tip. In order to avoid

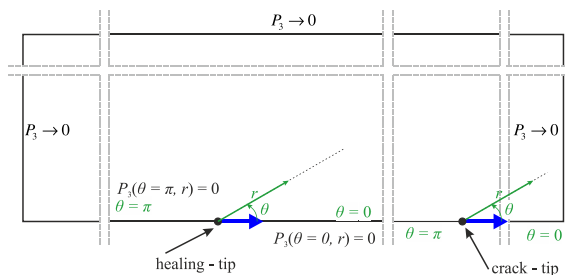


Fig. 21. The boundary conditions for the Polarization problem.

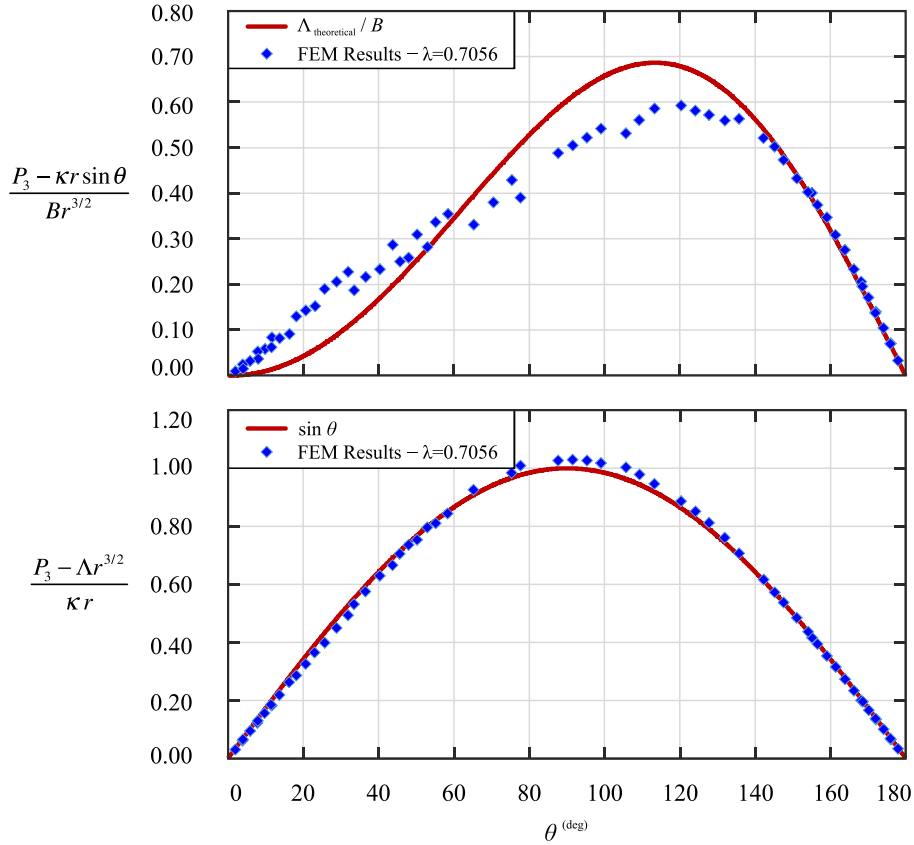


Fig. 22. (a) The influence of the term of order $O(r^{3/2})$, (b) The influence of the term of order $O(r^1)$. Note that in this example $B = 1.5610^{-2} m^{-1/2}$ was used (The estimation using eq. (37) gives $B = 1.6410^{-2} m^{-1/2}$). In this case, $2a/(\ell/\sqrt{2}) = 10$, $\tau_0/\mu = 1$ and $\ell/\sqrt{2} = 0.025/\sqrt{2}m$.

possible depolarization, the following equation should hold true, for the maximum polarization $P_3 = P_3^{max} = P_{max}$ (a material constant):

$$\left| c_1 \frac{\ell}{\sqrt{2}} \right| < P_3^{max} \quad (69)$$

Fig. 23 suggests that an increase of the rupture velocity will result in a concentration of polarization near the crack-tips. As the relative microstructure $2a/(\ell/\sqrt{2})$ increases, the normalized polarization decreases with ratio 1/2.

The maximum polarization depends on the shear stress, the crack propagation velocity, and the relative crack size $2a/(\ell/\sqrt{2})$. The critical combination of the previous parameters will occur for $V/c_s \rightarrow 1.00$. Table 2 depicts a critical loading leading to depolarization at the crack-tip for the materials of Table 1. As the relative microstructure increases, higher shear stress is required for depolarization, implying a depolarization strengthening effect.

6. Conclusion

The mode III, anti-plane, Yoffe-type, fracture problem was studied for flexoelectric materials. Initially the case of a non-flexoelectric material was studied using FEM. The stress intensity factor K_{III} of the Yoffe-type problem was found to be equal to that of the static problem. Increase of the rupture velocity resulted in increase of the crack sliding displacement. Aside from verifying numerically the available analytical results of classical elastodynamics, we found two additional analytical results regarding the asymptotic and the overall forms of the crack displacement field.

Next, the flexoelectric problem was studied, under elliptic conditions. The asymptotic displacement field was found to be of order $O(r^{3/2})$. However, we found an important (and more singular) term of order $O(r^1)$. Each of the terms contributes with a different angular variation around the tip, and a different amplitude. The angular variation of order $O(r^{3/2})$ was identical to that of the semi-infinite crack as calculated in our previous study [30] and is the only term that gives a positive J integral. The asymptotic field amplitudes were estimated numerically, and the energy release rate was found semi-analytically. The classical elastodynamic case predicts a monotonic increase of the J-integral with the rupture velocity, going to infinity for velocities near the shear wave speed. On the

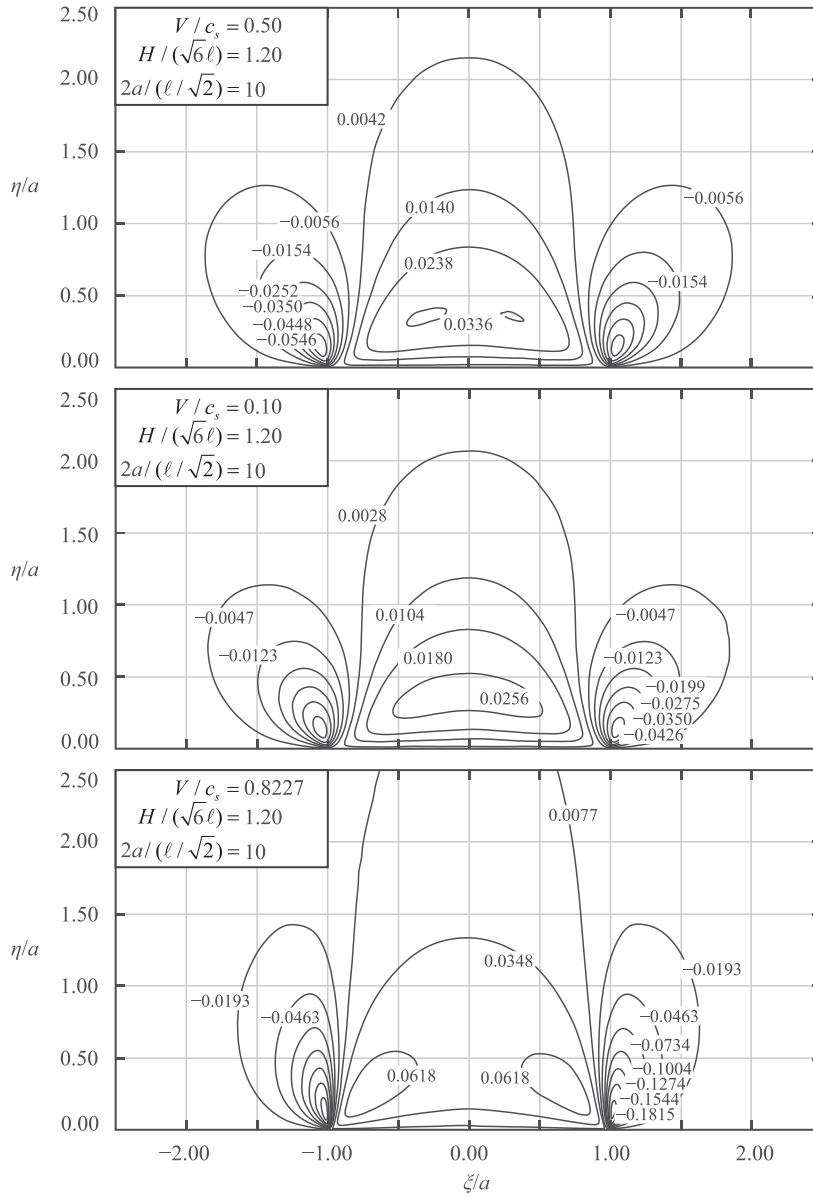


Fig. 23. Influence of the velocity V/c_s in the polarization $P_3(c_s^2 a^2 \mu) / [V^2 (e_{44} - f_{12}) 2a \tau_0]$ for $2a/(l/\sqrt{2}) = 10$

other hand, the flexoelectric case predicts a monotonic decrease of the J-integral, going to zero for $\lambda \rightarrow 1$. Interestingly, these results resemble the ones found for the classical elastodynamic case with the addition of a cohesive zone [7]. The displacement along the crack line reveals the formation of cusp-like crack-tip displacements at both crack tips, which depends on the microstructural length's ratio $H/(\sqrt{6}l)$ [20]. Flexoelectricity creates a stiffening effect.

The polarization field in an anti-plane, mode III, Yoffe-type, crack was investigated taking Faraday's cage – like boundary conditions. Anti-plane polarization is increasing with the rupture velocity and the microstructure, due to the increase of strain gradient, with rupture speed. The asymptotic polarization varies as $O(r^1)$. Neither the classical nor the flexoelectric Yoffe's type problem has a solution in the hyperbolic regime (supershear regime in the classical case). Many of our conclusions for the flexoelectric materials hold also for couple stress and dipolar elasticity theories that use equations similar to those of a flexoelectric material.

In reference [36], it was proposed that the polarization singularity is $O(r^{-1/2})$. While the procedure of [36] seems similar, there are many differences from our work. The most significant is that this study accepted the possibility that the displacement close field can have additional terms of different order than $3/2$. These terms do not contribute in the energy release rate, but can exist as long as they do not violate the integrability of eq. (1). Also, the decoupling of the polarization equation reveals higher derivatives of polarization, making the polarization singularity to be controlled by terms of order $O(r^1)$, justified by FEM results.

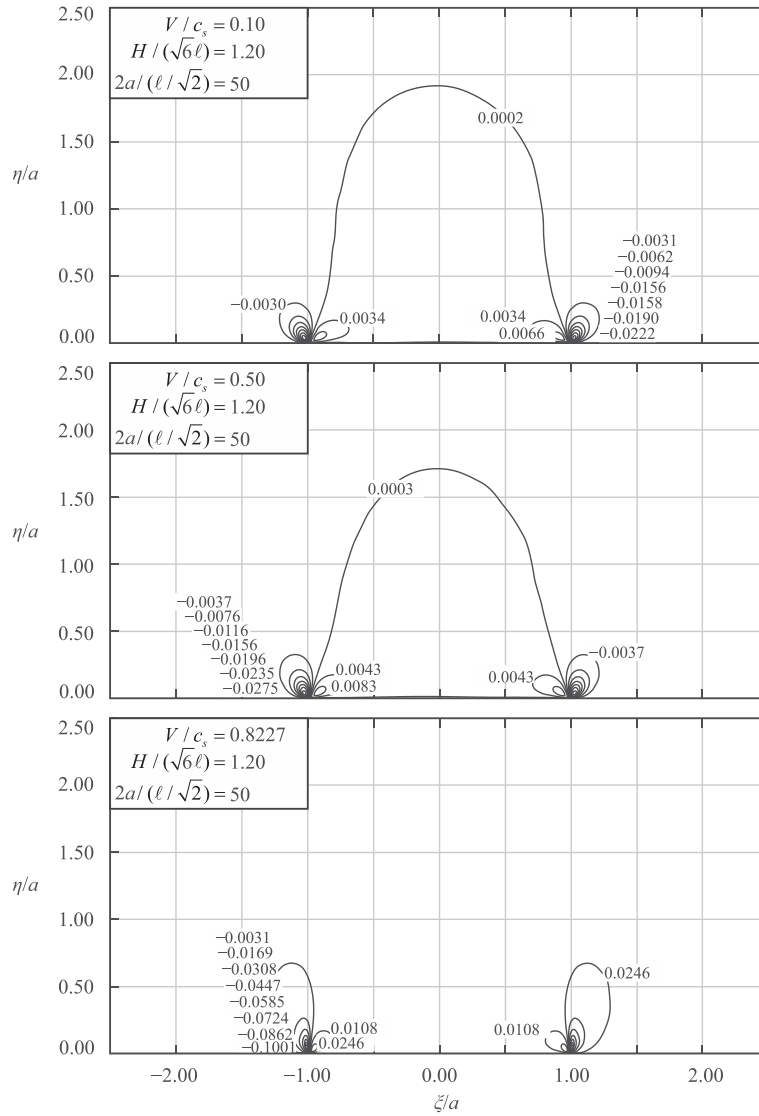


Fig. 24. Influence of the velocity V/c_s in the polarization $P_3(c_s^2 a^2 \mu) / [V^2(e_{44} - f_{12})2a\tau_0]$ for $2a/(\ell/\sqrt{2}) = 50$

Table 2
The critical shear stress for depolarization at the crack-tip.

	$\frac{V^2 \tau_0}{c_s^2 \mu} \frac{2a}{\ell/\sqrt{2}}$	$\frac{\max P_3 \ell^2}{\frac{e_{44} - f_{12}}{\alpha} \frac{V^2 \tau_0}{c_s^2 \mu}}$	$\max P_3 \left[\frac{\mu C}{\text{cm}^2} \right]$	$P_3^{\max} \left[\frac{\mu C}{\text{cm}^2} \right]$	$\text{crit} \left(\frac{V^2 \tau_0}{c_s^2 \mu} \frac{2a}{\ell/\sqrt{2}} \right)$	$\text{crit} \left(\frac{\tau_0}{\mu} \right)$
$2a/(\ell/\sqrt{2}) = 10$						
SrTiO ₃	6.768353	0.2	13.52	0.42	0.2102	0.0210
PMMA			37.13	0.57	0.1039	0.0104
KTaO ₃			68.92	0.24	0.0235	0.0024
$2a/(\ell/\sqrt{2}) = 50$						
SrTiO ₃	33.84176	0.1	0.071	0.42	199.8	3.996
PMMA			0.035	0.57	548.6	10.972
KTaO ₃			0.008	0.24	1018.2	20.364

CRedit authorship contribution statement

Ch. Knisovitis: Writing – original draft, Validation, Methodology, Investigation, Formal analysis, Data curation. **A.E. Giannakopoulos:** Writing – review & editing, Visualization, Supervision, Project administration, Methodology, Investigation, Formal analysis, Data curation, Conceptualization. **Ares J. Rosakis:** Writing – review & editing, Visualization, Supervision, Project administration, Methodology, Investigation, Formal analysis, Conceptualization.

Declaration of competing interest

The authors declare that they have no known competing financial interests or personal relationships that could have appeared to influence the work reported in this paper.

Appendix. . The anti-plane flexoelectric boundary conditions

Following [21,25,26] through the minimization of the total Energy Density, we get three Euler conditions for all the material point of the body: The conservation of linear momentum, the conservation of electric field and Maxwell equation outside and inside the body for the anti-plane formulation, considering zero out of plane body force and zero initial electric filed:

$$\mu(u_{3,11} + u_{3,22}) + (e_{44} - f_{12})(P_{3,11} + P_{3,22}) = \rho \frac{\partial^2 u_3}{\partial t^2} \tag{A.1}$$

$$-aP_3 + (e_{44} - f_{12})(u_{3,11} + u_{3,22}) + (b_{44} + b_{77})(P_{3,11} + P_{3,22}) = 0 \tag{A.2}$$

$$\Phi_{,11} + \Phi_{,22} = 0 \tag{A.3}$$

where Φ is the electric potential. Note that eq. (A.3) is independent of the other two.

Accordingly, we also get the mechanical boundary conditions of the original problem (eqs. (A.1) and (A.2)):

$$r_3 = f_{12}P_3 \quad \text{or} \quad u_{3,n} = \frac{\partial u_3}{\partial x_1}n_1 + \frac{\partial u_3}{\partial x_2}n_2 \tag{A.4}$$

$$t_3 = \mu u_{3,n} + (e_{44} - f_{12})P_{3,n} + \mu \frac{\partial^2}{\partial s^2} \left(\frac{\partial^2 u_3}{\partial x_1 \partial x_2} \right) \quad \text{or} \quad u_3 \tag{A.5}$$

$$\mu \frac{\partial^2}{\partial s^2} \left(\frac{\partial^2 u_3}{\partial x_1 \partial x_2} \right) \quad \text{or} \quad \frac{\partial u_3}{\partial s} \tag{A.6}$$

the polarization B.C.:

$$(b_{44} + b_{77})P_{3,n} + e_{44}u_{3,n} = 0 \quad \text{or} \quad P_3 \tag{A.7}$$

and also, the electric jump conditions (see [21,25,26]).

As proposed in in eq. (4) and (5), the problem decouples. More specifically we can differentiate eq. (A.2) with ∇^2 and substitute $(P_{3,11} + P_{3,22})$ from eq. (A.1) to find eq. (4), or substitute $(u_{3,11} + u_{3,22})$ from eq. (A.2) to (A.1) to find eq. (5). The same decoupling also carries to the boundary conditions. For example, the condition (A.5)(a) transforms to eq. (28)(a), by differentiating eqs. (A.1) and (A.2) with respect to the normal direction to the boundary.

Another way, to find the boundary conditions (28) can start from eq. (4), taking its weak form:

$$\int \left(\mu \nabla^2 u_3 - \mu \frac{\partial^2}{\partial s^2} \nabla^4 u_3 - \rho \frac{\partial^2 u_3}{\partial t^2} + \frac{\rho H^2}{12} \nabla^2 \frac{\partial^2 u_3}{\partial t^2} \right) \delta u_3 dx_1 dx_2 dt \tag{A.8}$$

After calculations this integral will result in path integrals which contain the boundary conditions as well as the initial conditions and area integrals which contain the elastic and the dynamic energy densities. Integral A.8 can be calculated as follows.

$$\iint (\nabla^2 u_3) \delta u_3 dx_1 dx_2 = \oint (u_{3,n} \delta u_3) \cdot \vec{n} ds - \iint \underbrace{(u_{3,n} \delta u_{3,n})}_{\substack{\text{Elastic} \\ \text{Energy} \\ \text{Variation}}} dx_1 dx_2 \tag{A.9}$$

$$\iint (\nabla^4 u_3) \delta u_3 dx_1 dx_2 = \oint \nabla [(\nabla^2 u_3)] \delta u_3 \cdot \vec{n} dS - \oint (\nabla^2 u_3) (\nabla \delta u_3) \cdot \vec{n} dS + \iint \underbrace{[(\nabla^2 u_3) (\nabla^2 \delta u_3)]}_{\substack{\text{Elastic Strain} \\ \text{Density}}} dx_1 dx_2 \quad (\text{A.10})$$

$$\int \frac{\partial^2 u_3}{\partial t^2} \delta u_3 dx_1 dx_2 dt = \int \underbrace{\left(\frac{\partial u_3}{\partial t} \delta u_3 \right)}_{\substack{\text{Initial} \\ \text{condition}}} dx_1 dx_2 - \int \underbrace{\left(\frac{\partial u_3}{\partial t} \frac{\partial \delta u_3}{\partial t} \right)}_{\substack{\text{Kinetic} \\ \text{Energy} \\ \text{Variation}}} dx_1 dx_2 dt \quad (\text{A.11})$$

$$\int \left(\nabla^2 \frac{\partial^2 u_3}{\partial t} \right) \delta u_3 dx_1 dx_2 dt = \oint \left[\left(\nabla \frac{\partial^2 u_3}{\partial t} \right) \delta u_3 \cdot \vec{n} \right] dt dS - \iint \underbrace{\left(\nabla \frac{\partial^2 u_3}{\partial t} \right) \cdot (\nabla \delta u_3)}_{\substack{\text{Initial} \\ \text{Conditions}}} dx_1 dx_2 dt \quad (\text{A.12})$$

Having in mind that the weak form becomes

$$\begin{aligned} & \int t_3 \delta u_3 dS dt + \int r_3 \delta u_{3,n} dS dt \\ & + \delta \int \text{Elastic Energy Density } dx_1 dx_2 dt \\ & + \delta \int \text{Kinetic Energy Density } dx_1 dx_2 dt \\ & + \int \text{Initial Conditions } dx_1 dx_2 dt \end{aligned} \quad (\text{A.13})$$

and that for our problem $\vec{n} = (0, n_2)$, we have

$$t_3 = \mu u_{3,2} - \mu \frac{\partial^2}{\partial x_2^2} (u_{3,22} + 2u_{3,11}) + \rho \frac{H^2}{12} \frac{\partial^2 u_{3,2}}{\partial t^2} \quad (\text{A.14})$$

taking into account the antisymmetry of the problem with respect to x_1 . Also, we get

$$r_3 = \mu \frac{\partial^2}{\partial x_2^2} u_{3,22} \quad (\text{A.15})$$

as well as, the following initial conditions ($t = 0$) $u_3, u_{3,1}, u_{3,2}, \partial u_3 / \partial t, \partial u_{3,1} / \partial t, \partial u_{3,2} / \partial t$.

Data availability

Data will be made available on request.

References

- [1] Giannakopoulos AE, Knisovitis C, Charalambopoulos A, Zisis T, Rosakis AJ. Hyperbolicity, mach lines, and super-shear mode III steady-state fracture in magneto-flexoelectric materials. Part I: Methodology J Appl Mech 2023;90:1–27. <https://doi.org/10.1115/1.4056914>.
- [2] Giannakopoulos AE, Rosakis AJ. Dynamic magneto-flexoelectricity and seismo-electromagnetic phenomena: Connecting mechanical response to electromagnetic signatures. J Mech Phys Solids 2022;168:105058. <https://doi.org/10.1016/j.jmps.2022.105058>.
- [3] Giannakopoulos AE, Rosakis AJ. Dynamics of flexoelectric materials: subsonic, intersonic, and supersonic ruptures and mach cone formation. J Appl Mech 2020; 87:061004. <https://doi.org/10.1115/1.4046634>.
- [4] Freund LB. *Dynamic Fracture Mechanics*. Cambridge University Press; 1990.
- [5] Yoffe EH. LXXV. The moving Griffith crack. The London, Edinburgh, and Dublin Philosophical Magazine and Journal of Science 1951;42:739–50. <https://doi.org/10.1080/14786445108561302>.
- [6] Freund LB. The mechanics of dynamic shear crack propagation. J Geophys Res 1979;84:2199. <https://doi.org/10.1029/JB084iB05p02199>.
- [7] Rice JR, Sammis CG, Parsons R. Off-fault secondary failure induced by a dynamic slip pulse. Bull Seismol Soc Am 2005;95. <https://doi.org/10.1785/0120030166>.
- [8] Georgiadis HG, Theocaris PS. The Keldysh-Sedov method for a closed-form elastodynamic solution of the cracked strip under anti-plane shear. Int J Eng Sci 1986;24:1135–40. [https://doi.org/10.1016/0020-7225\(86\)90008-X](https://doi.org/10.1016/0020-7225(86)90008-X).
- [9] Bhat HS, Dmowska R, King GCP, Klinger Y, Rice JR. Off-fault damage patterns due to supershear ruptures with application to the 2001 Mw 8.1 Kokoxili (Kunlun) Tibet earthquake. J Geophys Res Solid Earth 2007;112. <https://doi.org/10.1029/2006JB004425>.
- [10] Poliakov ANB, Dmowska R, Rice JR. Dynamic shear rupture interactions with fault bends and off-axis secondary faulting. J Geophys Res Solid Earth 2002;107. <https://doi.org/10.1029/2001jb000572>.

- [11] Ida Y. Cohesive force across the tip of a longitudinal-shear crack and Griffith's specific surface energy. *J Geophys Res* 1972;77:3796–805. <https://doi.org/10.1029/JB077i020p03796>.
- [12] Sih GC, Chen EP. Moving cracks in a finite strip under tearing action. *J Franklin Inst* 1970;290:25–35. [https://doi.org/10.1016/0016-0032\(70\)90057-8](https://doi.org/10.1016/0016-0032(70)90057-8).
- [13] Bilby BA, Bullough RLXXI. The formation of twins by a moving crack. *The London, Edinburgh, and Dublin Philosophical Magazine and Journal of Science* 1954; 45:631–46. <https://doi.org/10.1080/14786440608520468>.
- [14] Singh BM, Bryant Moodie T, Haddow JB. Closed-form solutions for finite length crack moving in a strip under anti-plane shear stress. *Acta Mechanica* 1981;38: 99–109. <https://doi.org/10.1007/BF01351465>.
- [15] Kwon SM, Lee KY. Constant moving crack in a piezoelectric block: anti-plane problem. *Mech Mater* 2001;33:649–57. [https://doi.org/10.1016/S0167-6636\(01\)00082-5](https://doi.org/10.1016/S0167-6636(01)00082-5).
- [16] Zhou Y-B, Li X-F. A Yoffe-type moving crack in one-dimensional hexagonal piezoelectric quasicrystals. *Appl Math Model* 2019;65:148–63. <https://doi.org/10.1016/j.apm.2018.08.005>.
- [17] Chen ZT, Yu SW. Anti-plane Yoffe crack problem in piezoelectric materials. *Int J Fract* 1997;84:L41–5.
- [18] Chen H, Ma J, Pei Y, Fang D. Anti-plane Yoffe-type crack in ferroelectric materials. *Int J Fract* 2013;179:35–43. <https://doi.org/10.1007/s10704-012-9767-2>.
- [19] Mindlin RD. Polarization gradient in elastic dielectrics. *Int J Solids Struct* 1968;4:637–42. [https://doi.org/10.1016/0020-7683\(68\)90079-6](https://doi.org/10.1016/0020-7683(68)90079-6).
- [20] Gavardinias ID, Giannakopoulos AE, Zisis T. A von Karman plate analogue for solving anti-plane problems in couple stress and dipolar gradient elasticity. *Int J Solids Struct* 2018;148–9. <https://doi.org/10.1016/j.ijsolstr.2017.07.026>.
- [21] Giannakopoulos AE, Zisis T. Steady-state antiplane crack considering the flexoelectrics effect: surface waves and flexoelectric metamaterials. *Arch Appl Mech* 2021;91:713–38. <https://doi.org/10.1007/s00419-020-01815-y>.
- [22] Georgiadis HG. The mode III crack problem in microstructured solids governed by dipolar gradient elasticity: static and dynamic analysis. *J Appl Mech* 2003;70: 517–30. <https://doi.org/10.1115/1.1574061>.
- [23] Morini L, Piccolroaz A, Mishuris G, Radi E. On fracture criteria for dynamic crack propagation in elastic materials with couple stresses. *Int J Eng Sci* 2013;71: 45–61. <https://doi.org/10.1016/j.ijengsci.2013.05.005>.
- [24] Maranganti R, Sharma P. Atomistic determination of flexoelectric properties of crystalline dielectrics. *Phys Rev B* 2009;80:054109. <https://doi.org/10.1103/PhysRevB.80.054109>.
- [25] Giannakopoulos AE, Zisis T. Uniformly moving antiplane crack in flexoelectric materials. *Eur J Mech A Solids* 2021;85:104136. <https://doi.org/10.1016/j.euromechsol.2020.104136>.
- [26] Giannakopoulos AE, Zisis T. Uniformly moving screw dislocation in flexoelectric materials. *Eur J Mech A Solids* 2019;78:103843. <https://doi.org/10.1016/j.euromechsol.2019.103843>.
- [27] Gourgiotis PA, Georgiadis HG. Distributed dislocation approach for cracks in couple-stress elasticity: shear modes. *Int J Fract* 2007;147:83–102. <https://doi.org/10.1007/s10704-007-9139-5>.
- [28] Eliseev EA, Morozovska AN, Glinchuk MD, Blinc R. Spontaneous flexoelectric/flexomagnetic effect in nanoferroelectrics. *Phys Rev B Condens Matter Phys* 2009;79. <https://doi.org/10.1103/PhysRevB.79.165433>.
- [29] Yudin PV, Ahluwalia R, Tagantsev AK. Upper bounds for flexoelectric coefficients in ferroelectrics. *Appl Phys Lett* 2014;104. <https://doi.org/10.1063/1.4865208>.
- [30] Giannakopoulos AE, Knisovitis C, Zisis T, Rosakis AJ. Hyperbolicity, mach lines, and super-shear mode III steady-state fracture in magneto-flexoelectric materials, part II: crack-tip asymptotics. *J Appl Mech* 2023;90:1–24. <https://doi.org/10.1115/1.4056913>.
- [31] COMSOL. *IEEE Microw Mag* 2021;22:7–7. <https://doi.org/10.1109/MMM.2021.3119712>.
- [32] Rice JR. The mechanics of earthquake rupture. *Physics of the Earth's Interior* 1980;78:555–649.
- [33] Erdogan F. *Crack Propagation Theories*. NASA CR 901. National Aeronautics and Space Administration 1968.
- [34] Palmer JR, Rice JR. The growth of slip surfaces in the progressive failure of over-consolidated clay. *Proceedings of the Royal Society of London A Mathematical and Physical Sciences* 1973;A332:527–48. <https://doi.org/10.1098/rspa.1973.0040>.
- [35] Andrews DJ. Rupture propagation with finite stress in antiplane strain. *J Geophys Res* 1976;81:3575–82. <https://doi.org/10.1029/JB081i020p03575>.
- [36] Tian X, Xu M, Zhou H, Deng Q, Li Q, Sladek J, et al. Analytical studies on mode III fracture in flexoelectric solids. *J Appl Mech* 2022;89:41006. <https://doi.org/10.1115/1.4053268>.